17 Direct-Reading Techniques Using Particle Motion and Optical Detection

PAUL A. BARON

Centers for Disease Control and Prevention*, National Institute for Occupational Safety and Health, Cincinnati, OH

MALAY K. MAZUMDER

Department of Applied Science, University of Arkansas at Little Rock, Little Rock, AR

YUNG-SUNG CHENG

Lovelace Respiratory Research Institute, Albuquerque, NM

INTRODUCTION

Optical direct-reading particle-counting techniques have the advantage of rapid, continuous, nondestructive particle detection. However, the amount of light scattered may not be directly related to the property that one wishes to measure. By combining the advantages of optical detection techniques with the manipulation of particle motion, several instruments have been developed that detect more specific properties of aerosol particles. The aerodynamic size of particles is used to describe the behavior of particles in gravitational settling, filtration, respiratory deposition, sampling systems, and so forth.

Measurement of aerodynamic size at one time could only be achieved by manually observing the settling velocity of individual particles. Subsequently, impactors allowed the measurement of size distributions on a routine basis, although gravimetric and/or chemical analysis still had to be carried out in the laboratory. With the advent of new technology (e.g., lasers and microcomputers), real-time measurements became possible. Several instruments were developed to measure aerodynamic size as rapidly and accurately as possible. These included the Electric–Single Particle Aerodynamic Relaxation Time (E-SPART; ***HOS***)** analyzer, the Aerodynamic Particle Sizer (APS; ***TSI***) and the Aerosizer (***TSI***). While the latter two instruments allow rapid determination of size distributions, they measure particle behavior largely outside the Stokes regime, and the recorded size must be corrected to give an accurate aerodynamic size of individual particles.

* Mention of company or product names does not constitute endorsement by the Centers for Disease Control and Prevention.

** See Appendix I for full manufacturer addresses referenced to the italicized three-letter codes.

Aerosol Measurement: Principles, Techniques, and Applications, Second Edition, Edited by Paul A. Baron and Klaus Willeke.

ISBN 0-471-35636-0

While the aerodynamic diameter describes the inertial properties, the electrostatic charge influences the electrodynamic behavior of the particle in transport processes. Both aerodynamic diameter and electrostatic charge measurements on individual particles are needed in many electrodynamic processes; some examples are electrophotography and laser printing, electrostatic powder coating, electrostatic precipitation, electrostatically enhanced fabric filtration, and electrostatic beneficiation of minerals and coal. The E-SPART is capable of measuring particle charge as well as aerodynamic diameter.

Airborne asbestos fiber measurements went through a similar progression over time in that, originally, relatively crude measurements of concentration were made by collection with midget impingers and microscope counting of all large particles. Filter collection with microscopic analysis was developed so that only fibers were detected. Finally, the development of the Fibrous Aerosol Monitor (model FAM-1, ***MIE***) allowed continuous, real-time detection of airborne fibers. The FAM-1 was designed to give results close to those of the phase contrast light microscopic method (see Chapters 12 and 26).

These sophisticated instruments provide more specific data about aerosols; however, because of the complexity of their detection and analysis systems, they may also have various limitations and subtle problems associated with the interpretation of the data. The following sections present a discussion of these instruments.

ELECTRIC–SINGLE PARTICLE AERODYNAMIC RELAXATION TIME ANALYZER

Measurement Principles

The Electric Single Particle Aerodynamic Relaxation Time (E-SPART) analyzer can be operated in several modes, the first of which is the original SPART mode (Mazumder and Kirsch, 1977; Mazumder et al., 1979). The SPART analyzer determines aerodynamic diameter by subjecting particles to an acoustic field of frequency f and measuring the response of these particles to the acoustic excitation. In its typical sampling configuration, the aerosol is sampled in a laminar air flow moving vertically downward through the SPART's sensing volume (Fig. 17–1). The acoustic field induces an oscillatory velocity component to the particle motion in the horizontal direction. The inertia of each particle causes a phase lag ϕ in the particle's periodic motion with respect to the acoustic field. This phase lag ϕ is related to the relaxation time of the particle τ_p, which is a function of the aerodynamic diameter d_a of the particle. The SPART analyzer employs a differential laser Doppler velocimeter (LDV) to measure the oscillatory velocity component (in the horizontal direction) of the particle and a microphone to measure the acoustic field. The phase lag of the particle motion with respect to the acoustic field driving the particle is converted to aerodynamic diameter using a microcomputer. The microcomputer stores the aerodynamic size data for the particles sampled and provides the measured size distribution. Although the response of the SPART can be calculated theoretically, it is calibrated with monodisperse latex particles because some instrumental parameters are difficult to measure.

In the E-SPART analyzer, an electrical particle acceleration field is used. There are two configurations: (1) a dc electric field superimposed on the acoustic field (Mazumder et al., 1983) and (2) an ac electric field replacing the acoustic field (Renninger et al., 1981). In the first configuration (i.e., an acoustic E-SPART analyzer), the horizontal motion of a charged particle is caused by the superposition of two fields: (1) the acoustic field forcing the particle in an oscillatory motion and (2) a dc electric field inducing a migration velocity component that depends on the polarity and magnitude of the electrical charge q of the particle and the field strength. In this configuration, d_a is measured for either electrically charged or uncharged particles by determining the phase lag ϕ. Electrical charge q is determined from

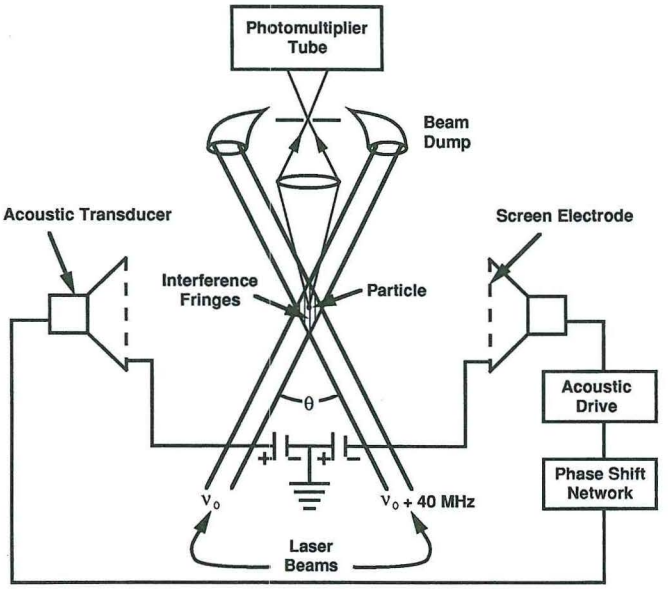

Fig. 17–1. Aerosol relaxation chamber showing the geometrical configuration of acoustic transducers and electrodes for applying acoustic and electric fields in the Electric–Single Particle Aerodynamic Relaxation Time (E-SPART) analyzer. One of the illuminating laser beams has been shifted by 40 MHz.

the measured electrical migration velocity V_e and the aerodynamic diameter d_a. The direction of V_e, which is also measured, provides the polarity of q.

In the second E-SPART configuration, no acoustic field is used, and the particles are subjected to an ac electric field. Therefore, the measurement process is applicable only to electrically charged particles. If a particle is charged, it experiences an oscillatory motion caused by the applied ac electric field. This oscillatory velocity component of the particle will have a phase lag ϕ with respect to the applied electric field, and measurement of ϕ again allows determination of d_a. The amplitude of the oscillatory velocity component of the particle is directly proportional to the electric charge on the particle. Thus, from the measurement of the velocity amplitude V_p and the phase lag ϕ, the electrostatic charge for individual particles can be calculated. There is a phase shift of 180° for particles of opposite polarity, and this 180° phase shift is detected to determine the polarity of the electrical charge. Both the phase lag and the amplitude information are obtained by the LDV and the associated signal processing electronics. More recently, applications of acoustic and electric drives to the measurement of particle size, charge, and density have been described (Cole, 1999; Cole and Tennal, 1993).

Particle Motion: External Oscillating Force

The oscillation of a particle experiencing a sinusoidal force F_e in a gaseous medium was derived by Stokes and can be represented in the Stokes regime by the following equation (Fuchs, 1964:80):

$$m_r \frac{dv_p}{dt} + \frac{v_p}{B_r} - F_e = 0 \qquad (17\text{–}1)$$

where m_r is the effective mass of the particle, B_r is the effective mobility of the particle, v_p is the time-dependent (instantaneous) particle velocity, and F_e is the external force. Because particle velocity is not constant, Stokes showed that m_r and B_r can be replaced by

$$m_r = m_p + \frac{9m'\xi}{4} \tag{17–2}$$

$$B_r = \left(\frac{3\pi\eta d_p}{C_c} + \frac{9m'\omega\xi}{4}\right)^{-1} \tag{17–3}$$

where m_p is the particle mass, η is the gas viscosity, C_c is the Cunningham slip correction factor, m' is the mass of air displaced by the particle, ω is the angular frequency of oscillation ($2\pi f$), and

$$\xi = \frac{2}{d_p\sqrt{2\nu/\omega}} \tag{17–4}$$

where ν is the kinematic viscosity (η/ρ_g), and ρ_g is the gas density. Equation 17–1 is a simplified version of the original Stokes equation for $m_p >> m'$. When the frequency approaches zero, that is, the velocity approaches a constant, ξ approaches zero and the effective particle mass can be replaced by m_p, B_r is reduced to the mobility B, and

$$F_r = -3\pi\eta d_p(V_p - U_g)/C_c \tag{17–5}$$

where V_p is the particle velocity and U_g is the steady-state gas velocity. This is the more familiar form of the Stokes equation.

Particle Motion: Acoustic Field. Equation 17–1 describes the motion of a particle under the influence of an external field, for example, a charged particle in an ac electric field. When there is no external field, but the medium itself is oscillating, for example, the particle experiences an acoustic excitation, the time-dependent gas velocity u_g can be expressed as

$$u_g = U_g \sin(\omega t) \tag{17–6}$$

where U_g is the maximum gas velocity and t is time. The parameters measured by the instrument are the velocity amplitude ratio

$$\frac{V_p}{U_g} = \sqrt{\frac{1 + 3\xi + \frac{9}{2}\xi^2 + \frac{9}{2}\xi^3 + \frac{9}{4}\xi^4}{\alpha^2 + 3\alpha\xi + \frac{9}{2}\xi^2 + \frac{9}{2}\xi^3 + \frac{9}{4}\xi^4}} \tag{17–7}$$

and the phase lag of the particle behind the air motion, given by

$$(\phi - \theta) = \tan^{-1}\left(\frac{3(\alpha - 1)\xi(\xi + 1)}{2\left(\alpha + \frac{3}{2}\alpha\xi + \frac{3}{2}\xi + \frac{9}{2}\xi^2 + \frac{9}{2}\xi^3 + \frac{9}{4}\xi^4\right)}\right) \tag{17–8}$$

where

$$\theta = \tan^{-1}\left(\frac{\frac{2}{3} + \xi}{\xi(\xi + 1)}\right) \tag{17–9}$$

and

$$\alpha = \frac{2\rho_p}{3\rho_g} \tag{17–10}$$

The right-hand sides of Eqs. 17–7 and 17–8 are described by the terms α, ξ, and ν, which are functions of the particle and gas properties. Figures 17–2 and 17–3 show $(\phi - \theta)$ and V_p/U_g, respectively, plotted as a function of aerodynamic diameter for several acoustic drive frequencies.

If the inertial terms caused by the acceleration of the particle in the medium are neglected, then particle motion can be represented using the particle relaxation time τ_p

$$\tau_p = \frac{\rho_o d_a^2 C_c}{18\eta} \tag{17–11}$$

where ρ_o is standard density (1000 kg/m^3 [1 g/cm^3]). The phase lag ϕ of the particle behind the air motion in the acoustic field is given by

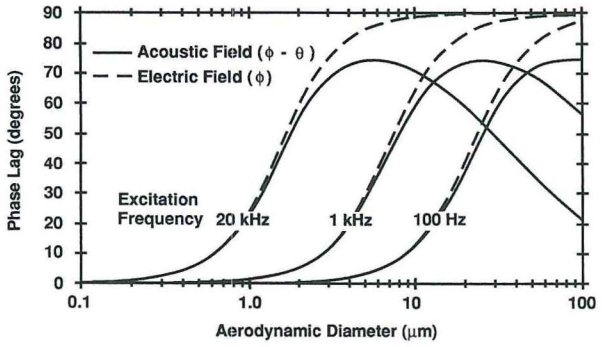

Fig. 17–2. Phase lag of the particle motion with respect to an acoustic excitation field (Eq. 17–8) and an electrostatic excitation field (Eq. 17–12) plotted as a function of aerodynamic diameter for several drive frequencies.

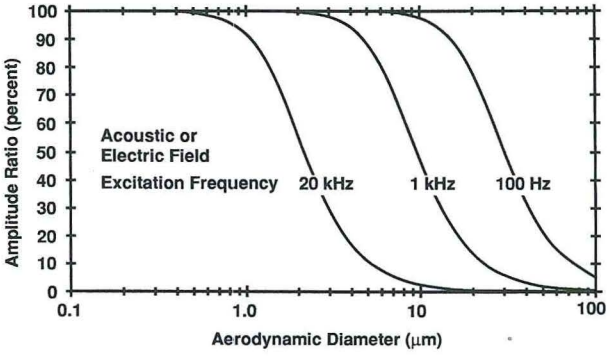

Fig. 17–3. Amplitude ratio of the particle motion with respect to an electrostatic field drive plotted as a function of aerodynamic diameter for several drive frequencies for the E-SPART (Eq. 17–7). The simpler equation (Eq. 17–13) gives similar curves throughout the entire range of sizes.

$$\phi = \tan^{-1}(\omega\tau_p) \tag{17–12}$$

where $\omega/2\pi$ is the acoustic frequency. The phase lag calculated using this equation is also plotted in Figure 17–2. Under this condition, the ratio of the amplitude of particle velocity V_p to the amplitude of the gas motion U_g due to the acoustic field is

$$\frac{V_p}{U_g} = \frac{1}{\sqrt{1+\omega^2\tau_p^2}} \tag{17–13}$$

Equations 17–11 and 17–12 can also be applied when the particle motion is induced by an external field, such as with a charged particle in an ac electric field. These equations, as well as Eqs. 17–7 and 17–8, indicate that the measurement of either the phase lag of the particle motion relative to the gas motion or the velocity amplitude ratio of the particle in the acoustic field is sufficient to determine τ_p or d_a.

In the case of acoustic excitation, there are two major forces acting on the particle besides gravitational field: (1) the viscous drag force and (2) the force caused by the pressure gradient in the medium. The first one is caused by the fluid resistance due to the viscosity of the medium, and the second is due to the inertial resistance. The effective fluid resistance will depend on the product $\omega\tau_p$. For small values of this product, the fluid resistance is primarily viscous, and for large values it is inertial. For sizing aerodynamic diameter, the product $\omega\tau_p$ can vary from 0.01 to 100. In the range 0.01 to 2, the resistance can be approximated by the viscous drag (Eq. 17–12), and, when $\omega\tau_p > 2$, both viscous and inertial resistance need to be considered (Eq. 17–8). Note that for $d_a \leq 100\,\mu m$, particle Reynolds number Re_p is less than 0.1.

The value of $\omega\tau_p = 2$ corresponds to $\phi = 63.5°$. For $\phi \leq 63.5°$, Eq. 17–12 gives results for an acoustic excitation within 15% of Eq. 17–8. For larger values of phase lag, the two curves are quite different (Fig. 17–2). However, the amplitude ratio curves given by Eqs. 17–13 and 17–7 are nearly identical (within less than 1%, Fig. 17–3), and, therefore, the simplified Eq. 17–13 holds over the entire range of $\omega\tau_p$.

To operate the analyzer over a wide size range, it is necessary to use two frequencies of excitation either in tandem inside a single relaxation chamber or simultaneously in two relaxation chambers connected in series. For example, a prototype E-SPART analyzer has been operated at two frequencies, 24 kHz (for 0.3 to 4.0 μm) and 1.0 kHz (for 2.0 to 20.0 μm), using two chambers connected in series. Integration of the experimental data can be accomplished with the appropriate software. The aerosol sampling system with only one relaxation chamber used in the E-SPART analyzer, is shown in Figure 17–4.

Particle Motion: dc Electric Field. When placed in a constant electric field E, the electrostatic force on a charged particle can be expressed as $F_e = qE$, where q is the particle charge. A particle of diameter d_a with n elementary charges will move with an electrical migration velocity V_e given by (see Chapter 3)

$$V_e = \frac{neEC_c}{3\pi\eta d_a} \tag{17–14}$$

where e is the elementary charge. As shown in Figure 17–3, the acoustic velocity component $V_p \sin(\omega t - \phi + \theta)$, is superimposed on this electrical migration velocity V_e. Figure 17–1 shows the geometrical configuration of transducers and electrodes for applying acoustic and electric fields. The field E is calculated from the voltage applied across the electrodes divided by the distance between them. Hence, a measurement of V_e can be used to calculate n, the number of elementary charges, once the aerodynamic diameter of the particle has been deter-

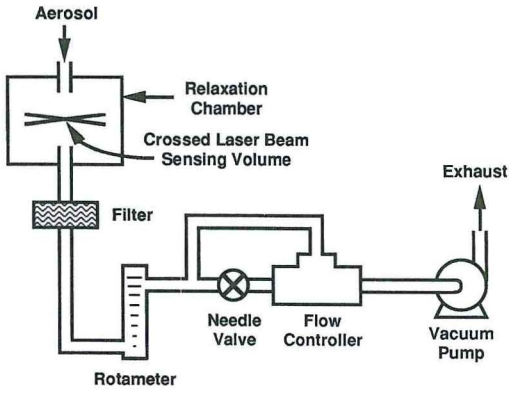

Fig. 17–4. A schematic of the aerosol sampling system used in the E-SPART analyzer.

mined. The software performing the charge measurement reads the voltage (which is adjustable) applied across the electrodes and computes the field E for determining the magnitude of the charge $q(ne)$ for each particle. The analyzer also recognizes the direction of V_e, which depends on the polarity of the charge q of the particle. Thus, from the direction and magnitude of V_e, the computer can record both polarity and magnitude of particle charge.

Particle Motion: ac Electric Field. The phase lag measurement technique can also be used on a charged particle in an ac E-SPART analyzer with the same electrode configuration shown in Figure 17–1 with no acoustic field applied. An electrical sinusoidal voltage $V_o \sin(\omega t)$ is applied across the two electrodes. In this process, it is necessary that the particles be electrically charged in order to make size and charge measurements. When a charged particle transits the LDV sensing volume, the particle will experience an oscillatory electric field, $E_o \sin(\omega t)$, and a zero gas velocity. When the time $t >> \tau_p$, ϕ has the same expression as Eq. 17–12, and the amplitude ratio is

$$\frac{V_p}{E_o} = \frac{qC_c}{3\pi\eta d_a \sqrt{1+\omega^2\tau_p^2}} \tag{17–15}$$

Equations 17–12 and 17–15 indicate that, for a charged particle, d_a can be determined from the measured value of the phase lag or the amplitude ratio as with the acoustical SPART analyzer.

In the case of electric excitation, there are two major forces acting on the particle besides the gravitational field: (1) the coulombic force and (2) the viscous drag force. For $Re_p < 0.1$, which is the case for many practical applications, the inertial resistance of the fluid can be neglected, and the phase lag is given by Eq. 17–12. Unlike acoustic excitation, there is no pressure gradient force, and hence there is no foldover in the phase lag relationship (Fig. 17–2). The amplitude ratio, in the case of either electric or acoustic excitation, is given by Eq. 17–13 without significant error. When $Re_p > 1$, appropriate correction will be needed to compute the viscous and inertial resistance forces acting on the particle for accurate size and charge measurements.

In the E-SPART analyzer, the measurement of d_a is independent of the driving field amplitude E_o and the magnitude of the particle charge q. Once d_a is determined from ϕ, the analyzer then calculates the electrical mobility ($q \cdot B$) or the electrostatic charge q of the particle from Eq. 17–15. The phase lag measurement technique is independent of the amplitude of

the driving force as long as the particle amplitude is sufficiently large for accurate measurement of ϕ.

E-SPART Analyzer

The E-SPART analyzer consists of four components: (1) a dual-beam, frequency-biased laser Doppler velocimeter; (2) a relaxation cell; (3) an electronic signal and data processing system; and (4) a personal computer. The LDV measures the particle velocity. The sensing volume of the LDV is formed by the intersection of the two laser beams and is located between the electrodes as shown in Figure 17–1. As a particle passes through the sensing volume in the direction normal to the plane containing the two converging laser beams, the particle experiences an acoustic and/or an electric field. The LDV detects only the horizontal velocity component of the particle. It does not detect the vertically downward sampling velocity. However, the duration of the LDV signal burst is the residence time of the particle within the sensing volume, and it is inversely proportional to the sampling velocity. The residence time must be long enough to measure $(\phi - \theta)$ and V_e or ϕ and V_p/E_o. The residence time is discussed further in "Aerosol Sampling."

A helium-neon laser (632 nm) or an argon-ion laser (488 nm) is used as the monochromatic light source for the LDV. The choice of laser (HeNe or Ar+) and the output power (10 mW for HeNe or 50 to 500 mW for Ar+) depends on the application. Two output laser beams are derived by passing the laser beam through an acousto-optic cell (Bragg cell) modulator. The output beams have nearly equal power, but one of the beams is shifted in frequency by 40 MHz by the modulator (Figure 17–1). The two beams intersect at the focal volume within the relaxation cell. Light scattered from aerosol particles passing through the sensing volume is collected by the receiving lenses and focused to a pinhole directly in front of a photomultiplier tube. The output of the photomultiplier is an electrical signal that represents the Doppler burst containing the particle motion information.

Aerosol Sampling

Figure 17–4 shows a schematic of the flow control system used for the E-SPART analyzer. The aerosol sample is drawn into the relaxation chamber by using a vacuum pump. A differential flow controller is used to maintain a constant rate of sampling flow approximately 0.5 L/min through the relaxation chamber. The sampling rate through the LDV sensing volume is a few milliliters per minute, depending on the specific optical configuration and the diameter of the particle. If the length of the sensing volume is L and the sampling velocity of the aerosol particles is V_z, then the maximum residence time of the particle in the sensing volume will be L/V_z. This residence time is set equal to $N \cdot t$, where N is the number of acoustic cycles and t is the time period of the acoustic or electric excitation. Under this condition, an aerosol particle passing vertically downward through the center of the sensing volume will undergo periodic motion for N excitation cycles. Phase lag ϕ measurements on each individual cycle for this particle can be performed by the E-SPART analyzer, and the average value of ϕ over N cycles is used to determine d_a.

The choice of N depends on three factors: (1) the size resolution desired, (2) the response time of the signal-processing electronics, and (3) the particle concentration. Typically, N is set between 3 and 8 by adjusting the sampling velocity V_z. Because the time period t depends on the frequency f of the acoustic or electric excitation drive, the residence time for particles is varied depending on f and the size measurements. All the particles may not pass through the center of the sensing volume, resulting in a shorter sensing time; however, the particle must stay in the volume for at least one cycle to be measured.

It is essential that a laminar flow field is maintained as the aerosol sample passes through and around the LDV sensing volume. Velocity components of the particle in the x direction

in the absence of any acoustic and electrical excitation should be less than the particle's Brownian motion.

Signal and Data Processing Electronics

The E-SPART signal-processing electronics are organized into five functional sections: (1) a receiver containing the RF amplifier, mixer, and demodulator; (2) the signal conditioning circuitry; (3) the size and charge measurement circuitry; (4) a direct memory access board for interfacing with the computer; and (5) a personal computer.

The instantaneous Doppler signal frequency generated by a particle traversing the sensing volume in the absence of any excitation is given by f_o, which is the LDV bias frequency (40 MHz) as determined by the Bragg cell. When a particle experiences an acoustic excitation of frequency f and a dc electric field, the Doppler frequency f_D is

$$f_D = f_o + \Delta f + \frac{2}{\lambda} V_p \sin(\omega t - \phi)\sin(\Theta/2) \tag{17–16}$$

where Θ is the intersection angle of the two laser beams, λ is the laser radiation wavelength, and ω is $2\pi f$. It is assumed ϕ is <63.5° in Eq. 17–16. A similar equation can be used when ac electric field excitation is used. The carrier frequency shift Δf is

$$\Delta f = \frac{2neEC_c}{3\pi\eta d_a \lambda}\sin(\theta/2) \tag{17–17}$$

where n is the number of electronic charges on the particles and E is the dc electric field.

In an acoustic E-SPART, the phase lag ϕ of the particle motion is determined from the time interval between the zero crossings of the acoustic field and the resultant particle motion (Fig. 17–5). The d_a for the particle is computed from f as follows:

$$d_a = \sqrt{\frac{9\eta\tan(\phi)}{\pi f \rho_o C_c}} \tag{17–18}$$

and from Eq. 17–17,

$$ne = q = \frac{3\pi\Delta f \eta d_a \lambda}{2EC_c \sin(\Theta/2)} \tag{17–19}$$

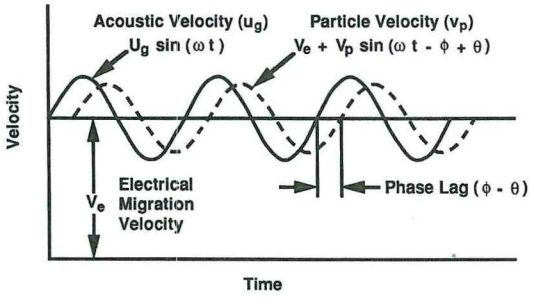

Fig. 17–5. Wave forms of the motion of charged particles within the sensing volume of the E-SPART analyzer.

In the case of the ac E-SPART, an ac electric field $E_o \sin(\omega t)$ replaces the dc electric field and the acoustic excitation. d_a is determined from ϕ, and q is calculated from the ratio of the amplitude of the particle motion (V_p) to the amplitude of the ac electric field E_o as shown in Eq. 17–15. The maximum value of the frequency deviation is

$$\Delta f_o = 2V_p \sin(\Theta/2)/\lambda \tag{17–20}$$

and

$$ne = q = \frac{3\pi|\Delta f_o|\eta d_a \lambda\sqrt{1+\omega^2\tau_p^2}}{2EC_c \sin(\Theta/2)} \tag{17–21}$$

The frequency deviation Δf_o, with respect to f_o, can be either positive or negative depending on the polarity of the charge. The magnitude of the charge is determined from $|\Delta f_o|$.

Table 17–1 shows a comparative analysis of two drive systems for the E-SPART analyzer: (1) Acoustic and DC Electric Drives and (2) AC Electric Drive. For such powder applica-

TABLE 17–1. Advantages and Disadvantages of Different Excitation Methods in the E-SPART Analyzer

Operational Features	Acoustic and DC Drive		AC Drive	
	Measurement of d_a	Measurement of q	Measurement of d_a	Measurement of q
Range of operation	From ϕ measurement in the range 0° to 70° (d_a can be measured from amplitude ratio [V_p/U_g])	From V_{TE} measurement in the range 0 to $\pm\, q_{max}$	From ϕ measurement in the range 0° to 90°	From V_p/E_o measurement in the range 0 to $\pm\, q_{max}$
Need for corrections	Stokes law does not remain valid when $\phi > 70°$ (no corrections are needed if amplitude ratio measurements are used)	Particle Reynolds number (Re) may exceed 1 for highly charged large particles	Stokes law can be applied without significant error	Particle Reynolds number (Re) does not exceed 1, even for the highly charged large particles
Counting efficiency and sampling error	Applicable to both charged and uncharged particles	Highly charged particles may be deflected away from the sensing volume	Applicable only to charged particles	No sampling loss caused by excitation
Change of size range/noise immunity	Change of acoustic drive frequency to change size range may need adjustments in electrode spacing	Flow turbulence and acoustically generated flow field affect q/m measurement	Range of operation can be changed continuously by changing frequency of the ac drive	No acoustically generated flow field noise. Measurement of q is insensitive to flow turbulence

tions as toners and powder coatings, the AC Drive System is more convenient for operating the instrument over a wide particle size range (Mazumder et al., 1999).

Instrument Operation

A data summary can be obtained that will provide the total number of particles counted with the average charge tabulated for a given size channel for both positive and negative charged particles. The software can provide plots of the size distribution of the aerosol in terms of number (Fig. 17–6), cumulative number, volume, cumulative volume, as well as statistics including count median diameter, mass median diameter, and geometric standard deviation.

For each particle, the aerodynamic diameter (d_a) and the charge (q) are determined in the E-SPART analyzer and the average value of the charge-to-mass ratio computed. For a spherical particle of diameter d_p and specific gravity ρ_p, we can write an approximate relationship:

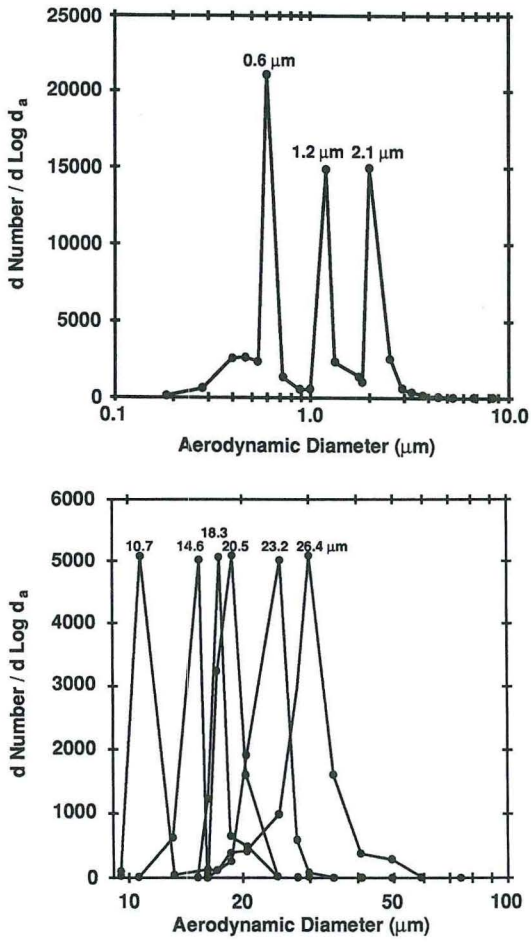

Fig. 17–6. **a**, Size frequency distribution $d\ N/d\log d_a$ for a mixture of polystyrene latex (PSL) spheres with diameters of 0.6, 1.2, and 2.1 µm (acoustic E-SPART). **b**, Size frequency distribution d $N/\mathrm{d}\log d_a$ for monodisperse bis-ethyl hexyl sebacate droplet aerosols of different sizes (ac E-SPART). The data were obtained to give equal peak concentrations.

$$d_p^2 \rho_p = d_a^2 \rho_o \tag{17–22}$$

The mass m_p of the particle can be computed from the measured value of d_a, if ρ_o is known. Thus,

$$m_p = \pi \rho_o^{3/2} d_a^3 / (6 \rho_p^{1/2}) \tag{17–23}$$

For each size channel $(d_a)_i$, from $i = 1$ to $i = 32$, the particle count is stored as n_i; m_p for each channel is approximately $\pi\, n_i\, \rho_o^{3/2}\, d_a^3/(6\, \rho_p^{1/2})$. The total mass of the particle sample is given by summing over i channels:

$$m = \sum (m_p)_i = \frac{\pi \rho_0^{3/2}}{6 \rho_p^{1/2}} \sum n_i (d_a)_i^3 \tag{17–24}$$

For each size channel, $(d_a)_i$, the total count n_i is also stored in the charge channels. The sums are performed over all 32 channels. The number of charged particles, n_i, is equal to $n^o + n_i^+ + n_i^-$ where n^o, n^+, and n^- represent the total number of particles with zero, positive, and negative charges with diameter $(d_a)_i$, respectively. The software provides computations and plots of n_i^+, n^o, n_i^-, versus charge-to-mass (q/m) ratio for any channel $(d_a)_i$, as shown in Figure 17–7. A three-dimensional plot of number versus charge-to-mass ratio and d_a is also available (Fig. 17–8).

Size Resolution. Particle size is measured by determining the phase lag ϕ between the particle motion and the driving force (acoustic or electric). In practice, a time interval Δt is measured, and the relationship between the phase lag ϕ and Δt is given by $\Delta t = \phi/\omega$. The signal-processing electronics determines Δt by generating a phase comparator pulse with the duration Δt and then counting the time period of that pulse using a counter of frequency f_c. To obtain good resolution, the counter frequency f_c is made many times larger than the excitation frequency f. The number of counts n_c for a given time interval Δt can be written as $n_c = \Delta t\, f_c$. Because the maximum value of phase shift is 90°, the maximum count will occur for a 90° phase shift. As shown in Figure 17–2, the variation of phase shift with respect to

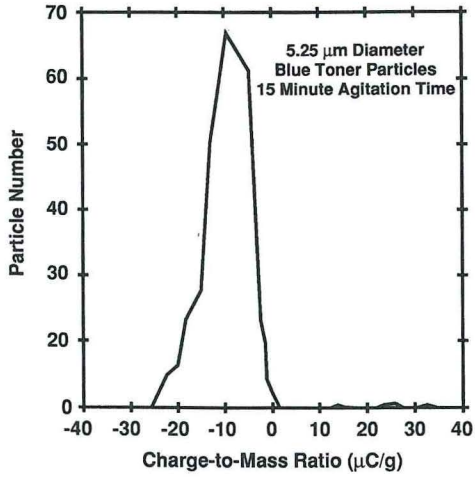

Fig. 17–7. Electrostatic charge distribution of a sample of blue toner showing the variation of charge density for a selected aerodynamic diameter.

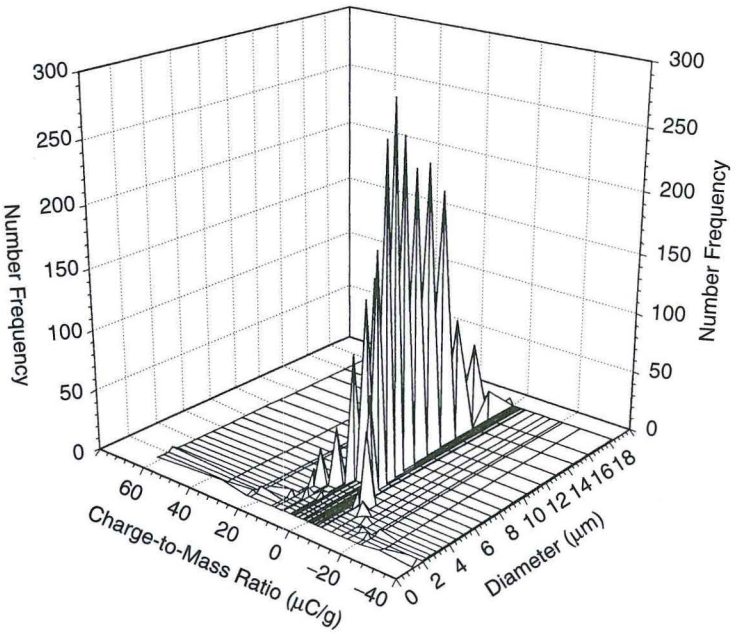

Fig. 17–8. A three-dimensional representation of the variation of particle count and charge density as a function of aerodynamic diameter.

aerodynamic diameter $d\phi/d(d_a)$ depends on the frequency of operation. For particles with the Cunningham correction factor equal to 1, that is, $d_a > 2\,\mu m$, maximum resolution (Renninger et al., 1981) is obtained when $d\phi/d(d_a)$ is maximum, which gives the phase angle $\phi = 30°$ or $\omega\tau_p = 1/\sqrt{3}$ for maximum resolution. In terms of channel number, the greatest resolution occurs when n_c is approximately equal to one third of the maximum count n_m. For example, it is possible to easily distinguish particle size differences between singlets, doublets, and triplets of 1.01 μm PSL particles.

Charge Resolution. The resolution in measuring particle charge also depends on the parameters of the instrument and the magnitude of the electric field. High-resolution charge measurement is needed to study the Boltzmann distribution of the particle charge. In such applications, a high electric field (dc) was used in the acoustic E-SPART, and the charge distribution was resolved within ±2.0 electronic charge, with the average charge varying from 0 to 50 electronic charges for 0.8 μm diameter monodisperse particles. For charged polydispersed particles, q/m measured using a Faraday cage agreed well with the q/m measured using the E-SPART. The resolution of the instrument is difficult to determine because there is no readily available process to control q accurately or any other instrument to measure the exact value of charge based on a single particle.

Range of Operation. The E-SPART analyzer can be operated in a range of 0.3 to 75 μm in aerodynamic diameter. The commercial instrument is operated at a single frequency. However, to cover this entire range, it is necessary to modify the analyzer to operate with at least two different frequencies of excitation, 25 and 0.5 kHz, in tandem or simultaneously. For high-resolution sizing of particles, it is necessary to operate the analyzer at three frequencies: 25, 2.0, and 0.5 kHz. The maximum particle count rate (10 particles/s to 2000 particles/s) depends on the frequency of operation.

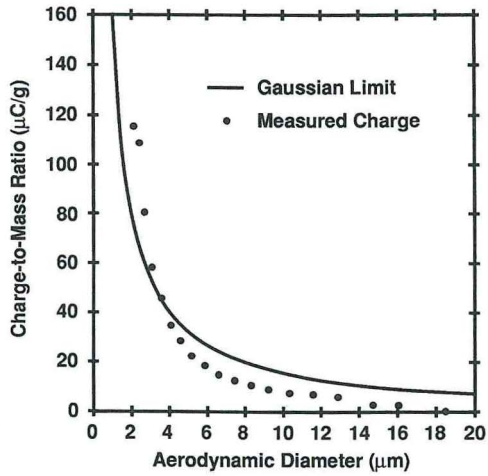

Fig. 17–9. The charge distribution of a tribo-charged toner sample as measured by an E-SPART analyzer. The solid line shows the saturation charge calculated from the Gaussian limit. The experimental data show that the E-SPART analyzer can measure particle charge near the saturation limit.

The desired range of measurement of electrostatic charge on each particle is from zero charge to its saturation value with positive or negative polarity. Figure 17–9 shows the average values of the charge-to-mass ratio of a toner sample experimentally measured as a function of d_a and the calculated Gaussian limit for maximum q/m as a function of diameter (Mazumder et al., 1991). The particles were tribo-charged. The saturation charge-to-mass ratio for tribo-charged, dielectric solid particles varies inversely with particle diameter. The data show that the analyzer can measure particles with saturation charge. For highly charged particles, the AC drive should be used to minimize sampling losses.

Precision and Accuracy. The basic principle applied in the E-SPART analyzer can provide absolute measurements of particle size and electric charge if the physical parameters involved are accurately known. For example, aerodynamic diameter depends on the viscosity of the gas in which the particles are suspended. Because viscosity is independent of pressure, the size measurement can be performed at different ambient pressures. However, if the temperature or the constituents of the gas change, the viscosity will change, and, therefore, the measured value of the aerodynamic diameter will be related to the properties of the gas in which the particles are suspended. This is an advantage of the E-SPART analyzer for in situ measurements. However, if there are uncertain variations in the ambient conditions from sample to sample, such as changes in temperature, the instrument's operation will be affected adversely. When the instrument is operated at a relatively high acoustic frequency (25 kHz), it is important to maintain a constant temperature in the relaxation cell so that the phase offset value does not change. This constraint is less severe when the acoustic E-SPART is operated at a frequency of 1 kHz or lower or is absent when an ac excitation is used.

AERODYNAMIC PARTICLE SIZER

The development of the Aerodynamic Particle Sizer (APS; ***TSI***) was based on a particle acceleration nozzle and laser Doppler detection system constructed by Wilson and Liu (1980). In this study particles were introduced into the center of an accelerating nozzle. Small particles followed the motion of the air closely while larger particles lagged behind, causing

an increase in relative velocity between air and particle. This increase in relative velocity is analogous to the increase in settling velocity with particle d_a. Wilson and Liu (1980) indicated that the particle velocity is a function of d_a as long as Re_p stays small (within the Stokes regime, $Re_p < 0.1$). As Re_p increases, apparent particle size becomes a function of particle density and shape as well as d_a. In addition, there is a trade-off in size resolution and nozzle velocity. At high nozzle velocities, particle motion is more non-Stokesian (less accurate aerodynamic sizing) but particle sizing is more rapid. Artifacts in the observed aerodynamic distribution may also occur because the light scattering used for detection of particles results in incomplete detection or particle coincidence.

Based on similar principles, ***TSI*** developed the APS with support from the National Institute for Occupational Safety and Health (NIOSH) (Agarwal and Remiarz, 1981). The APS sizes particles by measuring their velocity relative to the air velocity within an acceleration nozzle. This velocity is compared with a calibration curve established using monodisperse spheres. Several commercial models have been available over the past two decades:

Model 3300	Based on prototype design; used an Apple II computer for data analysis. HeNe laser light source (commercially discontinued)
Model 3310	Updated version of 3300 using an IBM PC-compatible computer for data analysis. Improved data display software. (commercially discontinued)
Model 3320	Particle acceleration system identical to other APS models, but using a solid-state laser and redesigned sensor package with integrated particle spectrum readout. Further data analysis and logging possible using external computer. Lower size resolution and better coincidence rejection than 3310. Light-scattering intensity data available
Model 3312	Particle sizing capability identical to Model 3320 (UV-APS), but with ultraviolet fluorescence and optical scattering signal information also available. Designed specifically for biologically based aerosols (also termed Fluorescence APS or FLAPS)

Instrument Description

The APS 3310 consists of a sensor unit containing the sampling system, detector, preliminary processing electronics and internal flow rate indicator, and a computer. The computer receives the data from the sensor unit about once per second and updates the calculated aerodynamic size distribution. One version of the software that collects and displays the data comes with the instrument; more sophisticated software providing near-real-time display is provided. While the entire unit is sufficiently portable and rugged that it can be used for field measurements (Baron, 1986; Baron and Willeke, 1986; Szewczyk et al., 1992), it is generally more suited to laboratory environments.

The APS 3320 sensing unit is more compact and can be used as a stand-alone unit, having a direct-reading display of the size distribution. The more compact sensor unit size and more stable flow system make it more amenable to field measurements than the 3310. For additional data analysis and recording of the data, a computer must be attached.

The inlet system and nozzle in all four APS models are identical. Aerosol is introduced to the inlet at a flow rate of 5 L/min. Four liters per minute of this flow is removed, passed through a filter, and reintroduced upstream of the acceleration nozzle as sheath air. The remaining 1 L/min aerosol flow is fed through a focusing nozzle, recombined with the sheath air, and accelerated through the final nozzle (Fig. 17–10). The pressure below the nozzle is approximately 100 mm Hg (Chen et al., 1985). The sheath and total flow are controlled by valves and monitored with thermal mass flow meters (3300 and 3310). The 3320 has microprocessor volumetric flow controllers for total and sheath flows.

At the exit of the acceleration nozzle, each particle passes through two light beams. The light comes from an HeNe laser in the 3310, while a laser diode (LD) provides illumination in the 3312 and 3320. The light scattered from the particle causes two pulses to be detected by a photomultiplier, and the time lag between the two pulses, representing time of flight (TOF) of the particle between the two beams, is recorded. Because larger particles have not accelerated to the air velocity in the sensing zone, they are represented by larger time lags. The TOF data are stored in an accumulator in bins representing equal time intervals.

In the 3310, two sets of data are stored: one by the small particle processor (SPP) in 4 ns bin intervals and the other by the large particle processor (LPP) in bin intervals of 66.7 ns. The software gives the option of using just the SPP for particle distributions in the range 0.5 to 15.9 μm, while the LPP can be used to extend that range up to 30 μm. The LPP has anti-coincidence circuitry that virtually eliminates excess counts due to coincidence. When both

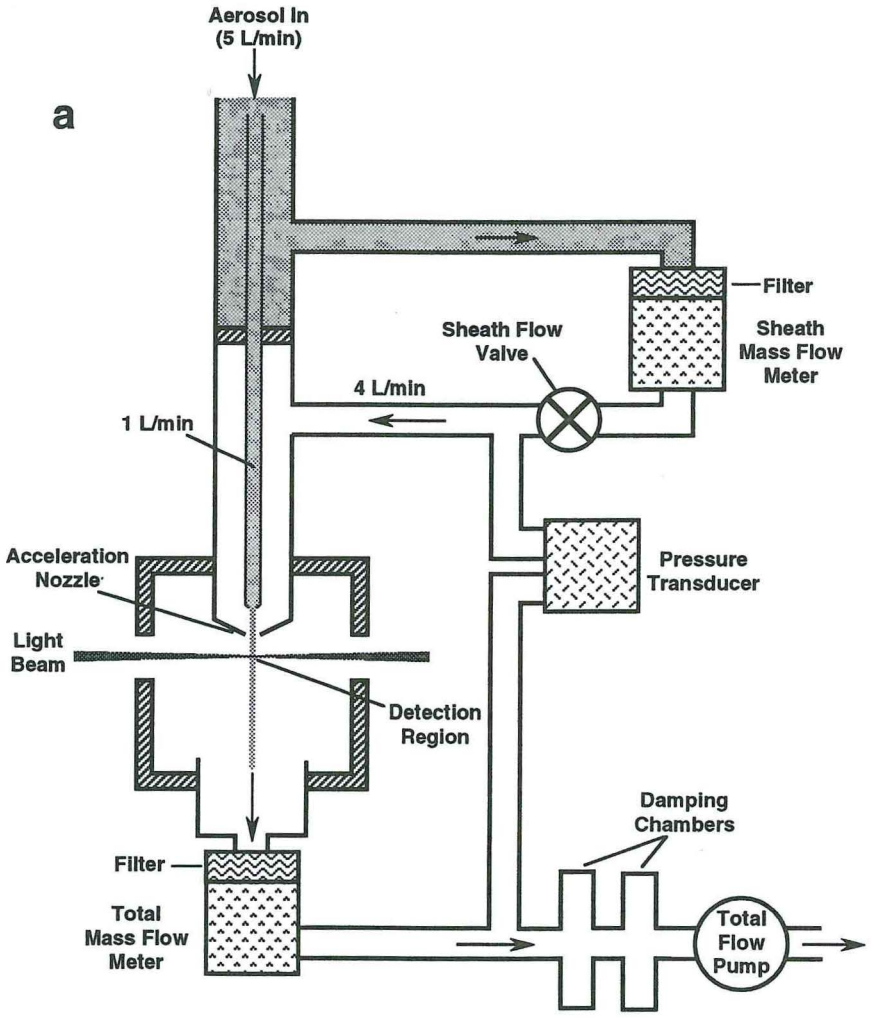

Fig. 17–10. Schematic of Aerodynamic Particle Sizer nozzle and laser velocimeter for models APS 3300 and 3310 (**a**) and for models APS 3320 and 3312 (**b**).

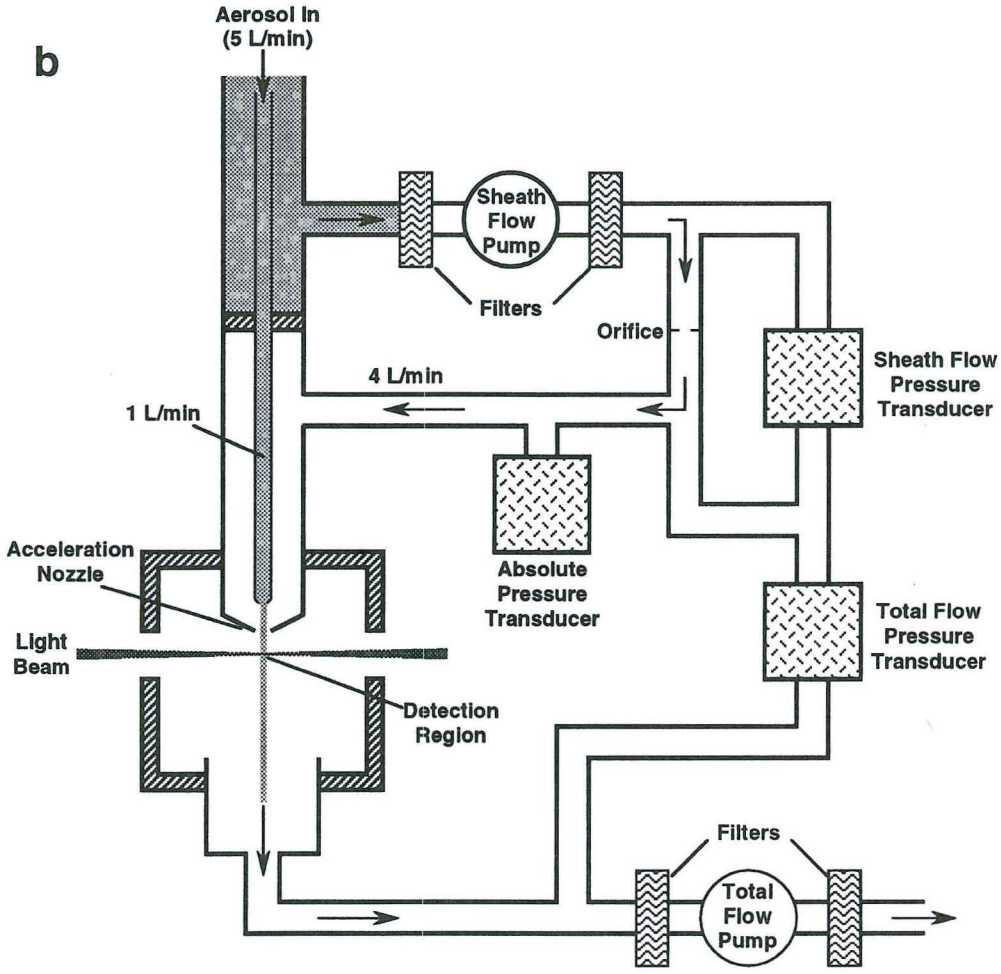

Fig. 17–10. *Continued*

processors are used, the two sets of data are linearly combined in the range from 5.7 to 15.9 μm.

In the 3320 and 3312, the LD illumination beams are relatively broad, and the light pulses overlap for each particle. The pulse shape is differentiated, and the inflection point of each peak defines the center point or mode of that peak. The light-scattering from each peak pair is measured and can be correlated to the TOF, allowing post process rejection of peak pairs whose heights do not correspond to the measured TOF. The light-scattering data are also available as a separate spectrum in the recorded data.

The final aerodynamic size is determined from a calibration of the accumulator spectrum using monodisperse spherical standard density (1000 kg/m^3) reference particles.

Sample Inlet

The 20 mm diameter inlet of the APS is located at the top of the instrument and is not conveniently located for sampling moving air directly. Thus, aerosols are typically ducted to the

APS with external tubing. Particle losses and aerosol nonuniformity within this tubing must be determined separately. Within the inlet, the air is split between the inner inlet (measured aerosol flow) and the sheath flow as indicated in Figure 17–10. The gas velocity at the measured flow inlet is higher than the velocity at the APS inlet (i.e., superisokinetic). This sampling arrangement produces some oversampling of larger particles to compensate for losses within the inner nozzle tube.

Aerosol entering the inlet is assumed to be uniform because only 20% of the aerosol is taken from the inlet stream and measured. Upstream manipulation of the aerosol stream, such as inertial stratification due to bends or cyclones, can bias the concentration at the measurement inlet. Careful mixing of the aerosol upstream of the measurement inlet may be necessary to reduce these effects with minimal losses.

Sample dilution systems are available as optional equipment for the APS to reduce problems with particle coincidence in the sensor. Penetration curves for these dilutors are measured by the manufacturer and are provided as part of the software to correct size distributions. At 15 μm the loss within the dilutor is near 50% and increases rapidly with increasing d_a; corrections of this magnitude indicate that larger particle channels provide data of questionable accuracy.

At the bottom of the inner inlet, a nozzle constricts the flow and focuses the aerosol in the center of the acceleration nozzle. The inner walls of the focusing nozzle form a 60° angle with the direction of flow. Impaction may produce particle accumulation on this nozzle surface, further restricting the penetration of the inner inlet to 50% for about 8 μm oil droplets (Kinney, 1990). Kinney et al. (1989) also evaluated modifications to this nozzle and found that a smaller nozzle angle (2° or 8°) produces less internal loss but decreases the resolution of the APS. The amount of particle loss for the 60° inlet nozzle can be approximated using an equation developed for particle deposition efficiency η in a tube with a 90° contraction.

$$\eta = [1 - \exp(1.721 - 8.557x + 2.227x^2)]^2 \tag{17–25}$$

where

$$x = \sqrt{Stk}/(D_i/D_n)^{0.31} \tag{17–26}$$

Stk is the Stokes number in the inlet tube, D_i is the diameter of the inlet tube, and D_n is the diameter of the nozzle (Ye and Pui, 1990). Impaction of liquid particles may follow the deposition efficiency described by Eq. 17–25, while solid particles may bounce and exhibit lower deposition.

Laser Velocimeter Sensor

Aerosol passing through the inner nozzle is combined with the sheath flow and focused into the center of the acceleration nozzle. The airflow conditions in the nozzle region have been modeled and agree well with experimental measurements (Ananth and Wilson, 1988). The air velocity reaches approximately 150 m/s at the exit of the acceleration nozzle. The flow conditions affecting the particle acceleration depend on the nozzle dimensions as well as the spacing of the nozzles. In the 3300 and 3310, the laser beam is split into two parallel, flattened beams that intersect the particle path 200 to 500 μm from the acceleration nozzle. The distance of these beams from the acceleration nozzle also affects the measured particle velocity. These various dimensions are difficult to control precisely during instrument manufacture. Thus, the calibration of each of these APS instruments is slightly different.

In the APS 3320 and 3312, the distance of the LD beam from the nozzle is more tightly

controlled during manufacture and can be reset without extensive recalibration. The sensor region is thus more accurately positioned, and the calibration from instrument to instrument should be more consistent.

Detection and Data Analysis

As each particle passes through the two laser beams, the pulses are detected by a photomultiplier and the TOF is recorded. Because the light scattered from particles changes rapidly with particle size, two high-speed data accumulator systems are used in the detector module of the APS 3300 and 3310: a small particle processor (SPP) and a large particle processor (LPP). The SPP collects the TOF data in an accumulator in increments of 4 ns, and the LPP collects data in increments of 66.7 ns. These data are passed from the detection module to a personal computer for transformation to size distribution according to a stored calibration curve, as well as for any further manipulation or storage as desired. The SPP covers the aerodynamic diameter range of 0.5 to 15.9 μm, and the LPP covers 5 to 30 μm. In the overlap range, the data from the two processors are blended together, proportionately increasing the LPP contribution with increasing size. The treatment of the overlap range is discussed further below in the section on coincidence.

The APS 3320 uses a single processor for particle detection. It can also correlate the particle velocity and light-scattering signal for post process rejection of particles whose velocities do not indicate particle sizes that match the observed light-scattering signal. For example, a particle with a low velocity (indicating a large particle) that produced a small scattering signal could be rejected as not being physically reasonable. This correlation changes for particles with different refractive indices. Once a number distribution has been measured, various other differential and cumulative distributions can be calculated in a similar fashion to those described for the E-SPART in the previous section.

Calibration

Monodisperse latex spheres are typically used for calibration of the full size range of the APS if it is to be used for measuring solid particles. Latex spheres smaller than about 5 μm can readily be generated by nebulizing a water suspension of the spheres. Note that while isopropyl alcohol suspensions of latex spheres may be easier to generate and dry, the alcohol slowly dissolves in the spheres and will cause a slight increase in size after a period of time. Larger calibration particles can be generated dry from a surface by suction, as with the Small Scale Powder Disperser (Model 3433, ***TSI***) or by gently brushing the calibration particles from a clean surface, such as a glass slide. Because latex particles are only available in specific sizes, the calibration curve is completed using a spline or polynomial function to fit the calibration points.

The calibration of each APS 3300 and 3310 instrument is unique due to variations in the nozzle sizes, spacing, and laser beam locations. However, once the calibration of the APS has been completed in air at ambient pressure, calibration for other gas viscosities and pressures can be achieved as described by Rader et al. (1990). The gas velocity U_g in the nozzle can be calculated from the Bernoulli equation for compressible flow:

$$U_g = \left[\frac{2RT}{M}\ln\left(\frac{P}{P-\Delta P}\right)\right]^{1/2} \tag{17–27}$$

where R is the universal gas constant, T is the absolute temperature, M is the gas molecular weight, P is the ambient pressure, and ΔP is the pressure drop across the nozzle. ΔP is measured by the flow transducer in the APS. The particle velocity V_p can be determined from

$$V_p = \frac{U_g t_{min}}{t} \tag{17-28}$$

where t is the transit time of the particle between the laser beams and t_{min} is the minimum transit time for small particles observable in the APS accumulator. Plotting the ratio V_p/U_g as a function of Stokes number results in a universal response curve. This means that the check on the APS size response under the same or new pressure or viscosity conditions can be achieved always setting U_g to the same value.

The design of the APS 3320 detection system is more compact and precise, resulting in reproducible spacing of the particle acceleration and illumination components. These components can be replaced by the user without the extensive factory recalibration procedure required with the earlier models. The APS also has a second pump that helps regulate the sheath flow. This results in less sensitivity to external pressure changes.

The flow system in the APS 3300 and 3310 is not as carefully controlled as in the APS 3320. Slight changes in pressure at the inlet of the earlier APSs could cause significant shifts in the apparent size distribution of submicrometer particles. The pressure drop change produced a slight shift in the flow through the acceleration nozzle, resulting in a slight change in the calibration curve as noted above. The channels in the submicrometer range were especially sensitive to slight changes in the calibration. The increased pressure drop shifted the calibration, decreasing the measured concentration of the smallest particles. This would become especially apparent when comparing size distributions upstream and downstream of a classifier (e.g., cyclone or impactor) that had small but measurable pressure drops. The ratio of the downstream to upstream concentrations could drop as low as 50% in the submicrometer range. The improved flow control in the APS 3320 sheath flow reduces the likelihood of such a calibration shift with small inlet pressure changes.

Other monodisperse particles, such as those generated from the vibrating orifice monodisperse aerosol generator (model VOMAG, ***TSI***) can also be used for calibration. However, it was found that oil droplets generated in this fashion distorted into oblate spheroids due to the high acceleration (see below) and therefore exhibited a smaller aerodynamic diameter than predicted for a spherical shape (Baron, 1986). Unless the calibration is used for measuring droplets of the same oil, only solid particles should be used for the particle size calibration of the APS.

Non-Stokesian Corrections

The acceleration in the nozzle produces Reynolds numbers outside the Stokes regime, as indicated in Table 17–2 for particles in the APS size range. Thus, the measured size depends on

TABLE 17–2. Particle Properties in the APS Nozzle

Particle Diameter (μm)	Relative Velocity (cm/s)	Particle Reynolds Number	Weber Number (Oil Droplets)[a]
0.5	40	0.013	2.9×10^{-6}
1.0	1,750	1.16	0.0113
3.0	6,490	12.9	0.468
10.0	10,600	69.6	4.13
15.0	11,500	114.0	7.36
20.0	12,300	163.0	11.2

[a]These represent either oleic acid or di-octyl phthalate, both of which have a surface tension of about 0.033 N/m [33 dyne/cm].

Source: Baron (1986).

other factors besides the aerodynamic size, including gas density, viscosity, particle density, and particle shape. Using the approach of Wang and John (1987), correction factors for the measured size of compact particles can be calculated if the particle density, gas density, and gas viscosity are known. These calculations have been validated by the Navier-Stokes calculation of the flow field in the APS nozzle by Ananth and Wilson (1988). The following equations (Rader et al., 1990) are iterated until no further significant change occurs.

$$\sqrt{Stk_2} = \sqrt{Stk_1}\left(\frac{6+R_2^{2/3}}{6+R_1^{2/3}}\right)^{1/2} \tag{17–29}$$

$$R_1 = \xi_i^{3/2}\sqrt{Stk_i}\,|U_g - V_p| \tag{17–30}$$

$$\xi_i = \left(\frac{18\rho_{gi}^2 S}{\rho_{pi}\mu_i U_g}\right)^{1/3} \tag{17–31}$$

where subscript 1 refers to calibration conditions with unit density spheres, subscript 2 refers to measurement conditions, Stk is the Stokes number, and S ($= U_g t_{min}$) is the distance between the laser beams. Measurements were made in argon and N_2O to confirm that this approach improved the accuracy of aerodynamic size measurement (Lee et al., 1990; Rader et al., 1990). The largest error in d_a (12%) was noted when these corrections were applied to large (30 μm) particles in argon. The slip correction factor must also be modified in the above equation because of the reduced pressure in the nozzle, and computer code is available to perform these corrections (Wang and John, 1989).

The high acceleration in the APS nozzle may also cause inaccuracies in measuring the d_a of nonspherical particles. Cheng et al. (1990) found that the measured size decreased with increasing shape factor. The above iterative correction was further modified to include shape factor. For more extreme shapes such as fibers, this approach may not be adequate. Identical-diameter fibers with different lengths gave the same measured size. Fibers, as well as other nonspherical particles, tend to orient themselves with their maximum cross section oriented perpendicular to the flow (Clift et al., 1978:142). However, larger fibers (on the order of 10 μm diameter) may not have sufficient time to orient in the flow field and may produce a measured size intermediate between the perpendicular and parallel orientation. Thus, the initial conditions of the particle (e.g., orientation, location in the flow field) during acceleration can affect the measured aerodynamic size.

The APS allows the rapid, precise measurement of aerodynamic size of most particles. Due to non-Stokesian flow in the acceleration nozzle, various factors bias that measurement. As described above, the biases caused by particle density, particle shape factor, gas viscosity, and gas density are sufficiently well understood that corrections to measured size can be made. The size of these biases is often on the order of 25% or less. Thus for many purposes, an estimated value of the particle density can yield sufficient accuracy in the corrected aerodynamic size. An exception may occur when the dynamic shape factor of the particle is large, as with fibers.

Chen and co-workers (1990) suggested that the correction factor for density is sufficiently well characterized that it can be used to provide estimates of aerosol particle density. Brockmann and Rader (1990) also used the APS response to measure shape factors for several types of particles.

Droplet Deformation

As indicated above, the high acceleration field in the APS will distort droplets into oblate spheroids with the maximum cross section perpendicular to the direction of motion, increasing the drag and causing them to be recorded as smaller particles. Figure 17–11 shows two

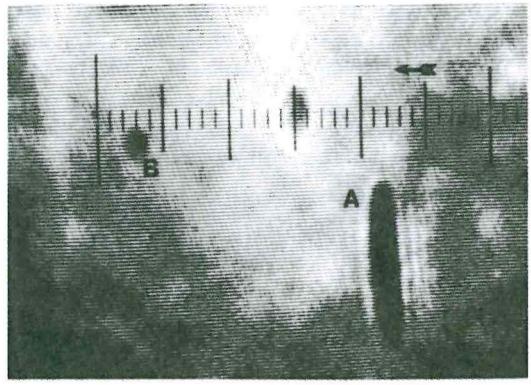

Fig. 17–11. Picture of droplets in the high-velocity air jet just beyond the APS nozzle taken with a high-speed laser-imaging system showing a droplet flattened by the drag force. The nozzle tip is about 200 μm to the right of droplet A, with the air and the droplets moving to the left. The scale markers are approximately 5 μm apart. The larger droplet A has an extreme 10 by 60 μm spheroidal shape, while the smaller droplet B is about 8 by 10 μm and is only slightly flattened.

dioctyl phthalate droplets detected with a laser imaging system (***LAS***) just past the tip of the acceleration nozzle. Air motion is directed from right to left, causing the deformation of the larger droplet into an extreme oblate shape and increasing the droplet drag. The flattened droplets in Figure 17–11 indicate that an oblate spheroidal shape is produced. The shape is not a true ellipsoid because the surface tension limits the curvature at the rim of the distorted droplet.

The distortion of a droplet in the sensing zone will depend on droplet size, the liquid surface tension, and viscosity. The Weber number, $We = u^2 \rho d_p / \gamma$, where u is the particle velocity relative to the air and γ is the droplet surface tension, represents the ratio of the air pressure force to the surface tension force. Droplets will eventually break up when experiencing Weber numbers between 12 and 20. Distortion increases with droplet size because the force on the droplet increases with size. While the Weber number indicates the maximum distortion that the droplet can undergo, the droplet viscosity determines the rate at which the droplet distorts. The rapid acceleration in the APS nozzle usually precludes droplet break up before reaching the sensing zone. Because the acceleration is high, viscosity is the controlling factor for distortion of many liquids (Griffiths et al., 1986). The degree of distortion has been calculated and agrees well with experimental measurements of the droplet undersizing for several oils with different viscosities (Bartley et al., 2000). Water droplets, which have a low viscosity but relatively high surface tension, distort less in the acceleration field (Baron, 1986; Bartley et al., 2000). In addition, the degree of distortion depends on the precise acceleration history and therefore can vary from instrument to instrument.

Coincidence Effects (APS 3310)

Accurate detection of a particle in the TOF detection system of the APS requires full detection of two pulses from the same particle. The coincidence effects resulting from such a system are more complex than those of a standard optical particle counter, where two coincident particles produce one somewhat larger measured particle. For the APS 3300 and 3310, several coincidence scenarios are presented in Figure 17–12. Coincidence between two particles can result in two smaller particles (Fig. 17–12a), one smaller particle, one randomly sized particle (Fig. 17–12b), or no particles (detected). The relative frequency of these possible

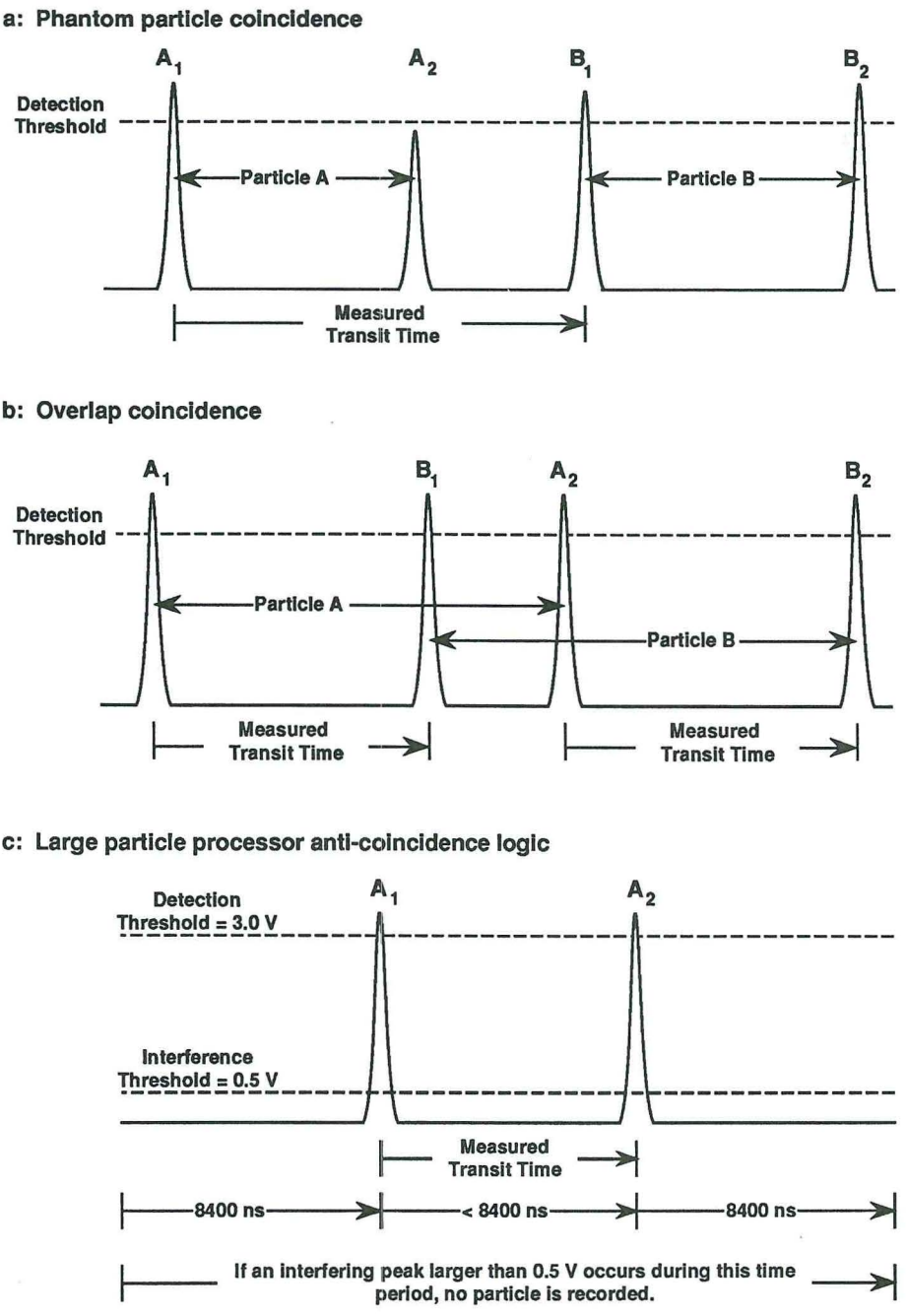

Fig. 17–12. Coincidence scenarios in the small particle processor (SPP) and the large particle processor (LPP) in the APS. **a**, A single detected pulse triggers the timer, while a pulse from a second particle produces a measured transit time that may indicate a particle of random size. **b**, Overlap of the pulses from two coincident particles produces two smaller detected particles. **c**, A particle detected by the LPP must have pulses larger than 3 V. The LPP anti-coincidence circuitry prevents detection of a particle when an interfering pulse occurs within 8400 ns before or after the evaluated pulse pair. (Adapted from Heitbrink et al., 1991.)

coincidence results and the effect on the measured distribution depends on the shape of the size distribution, the particle concentration, and which of the two signal processors (SPP or LPP) is used to detect the particles. The LPP is designed to completely eliminate coincidence counts (Fig. 17–12c) in the large particle range where coincidence can produce relatively large changes in apparent concentration. The coincidence effects in the APS 3310 have been modeled mathematically as well as with a Monte Carlo calculation (Heitbrink et al., 1991).

Particle-counting systems are prone to detection problems when more than one particle is present, or coincident, in the detection volume at the same time. The number of coincidence events in a measured distribution can be estimated from the difference between the actual concentration C_a and the measured concentration C_m:

$$C_a - C_m = C_a[1 - \exp(-C_a Q t)] \tag{17–33}$$

where Q is the flow rate through the detection volume and t is the residence time of the particle in the detection volume (Willeke and Liu, 1976). This equation can be used to estimate the APS coincidence loss to the peak of a monodisperse size distribution. Obtaining an accurate coincidence level for most size distributions is more difficult because it depends on particle size. For instance, the concentration giving 1% coincidence in the SPP for 0.8, 3, and 10 μm particles is approximately 560, 390, and 230 particles/cm^3, respectively. For the LPP, a 1% coincidence level is predicted for 10, 20, and 29 μm particles at concentrations of 55, 48, and 43 particles/cm^3 (TSI Inc., 1987). By using Eq. 17–33 with several particle sizes, the upper limit to the number of coincidence events can be estimated for broader size distributions.

C_a may also be difficult to estimate for many distributions where many of the particles detected by the SPP are smaller than 1 μm. These particles may be only partially detected, resulting in single detected pulses that contribute to coincidence events (Fig. 17–12a), but not to the observed small particle concentration. These coincidence events result in a randomly sized "phantom" particle. The result is a nearly constant background of these coincidence-induced phantom particles (Heitbrink et al., 1991).

The phantom particle background produced by the SPP is therefore dependent on the number of particles near the pulse detection limit of the sensor as well as the concentration of fully detected particles. This background becomes important in size regions where relatively few real particles are detected. Thus, when particle number distributions are converted to mass distributions, a few large phantom particles can bias the calculated mass and unrealistically skew the distribution (Baron, 1986). Another situation arises when two particle distributions are being compared, such as before and after a filter to measure penetration efficiency (Wake, 1989). In the size range where phantom particle concentration is more than a few percent of the real particle concentration, the ratio of the upstream and downstream distributions will be inaccurate.

The SPP thus tends to produce overestimates of particle concentration near the tail of a distribution, such as often occurs at large particle sizes. On the other hand, the LPP is designed to completely eliminate phantom particles (Fig. 17–12c). Therefore, coincidence results solely in a loss of LPP-detected particles. The difference between the LPP and the SPP concentration in the overlap range can give a hint of the magnitude of coincidence effects. The SPP coincidence can sometimes be reduced by lowering the photomultiplier gain. For size distributions skewed to small particle sizes, this reduces the number of small particles detected, thus reducing the phantom particle creation. If a region of the size spectrum is known not to contain any real particles, the detected particles can be assumed to be phantom particles created by coincidence. The average detected particle number per channel in this region can be subtracted from the entire distribution to obtain a more accurate distribution.

Coincidence Effects (APS 3312, 3320)

In the APS 3312 and 3320, the detection circuitry rejects all particles that may have experienced coincidence, much the same as with the APS 3310 LPP described above. This causes a reduction in observed particle concentrations that is likely to increase with particle size, because the detection time for larger particles is increased. The number of coincidence events is recorded and provided to the user. The number of single pulses is also recorded and used to indicate the bin below the lowest fully measured particles. These reported values should aid in estimating the importance of coincidence events. Further research is needed to allow a quantitative estimate of the change in the measured size distribution due to particle coincidence.

Resolution and Accuracy

As noted above, the APS measures particles largely outside the Stokes regime and requires corrections to the data to provide an accurate d_a. As with any complex instrument, frequent size calibration provides additional confidence in the accuracy of the results (see Chapter 21). Measurement of spherical particles can be corrected largely by taking into account particle density and, if necessary, changes in sampled gas density and viscosity. Liquid particles can also be accurately measured if calibrated with the same liquid. The resolution for spherical particles is high. For example, Remiarz et al. (1983) found geometric standard deviations in the range of 1.0058 (6.8 μm oil) to 1.025 (0.8 μm latex) for monodisperse particles using the APS prototype instrument. The particle size resolution of the APS 3320 is lower than in the previous models due to the poorer velocity measurement precision with the relatively broad LD light beams.

Due to non-Stokesian behavior and variations in the acceleration flow field experienced by particles approaching the detection region, resolution and accuracy may be diminished for nonspherical particles. If these are not corrected, the measurement accuracy will decrease. Marshall et al. (1991) found that the d_a of particles with a shape factor of 1.19 was underestimated by 25% in the APS.

Applications

The APS 3300, 3310, and 3320 can be used to measure size distributions in a variety of applications. These instruments have been combined with an electrical sizing instrument (see Chapter 18) to obtain size distribution measurements over a wide size range (0.02 to 30 μm). Sioutas et al. (1999) found reasonably good agreement between calculations of mass concentration from APS spectra and direct mass measurements in the size range of 0.5 to 9.2 μm. Peters et al. (1993) found good agreement between APS size distribution measurements and low pressure impactor measurements (see Chapter 10).

The APS has been used for bioaerosol measurement (Baron and Willeke, 1986). Specific detection of biologically based particles has been enhanced using the APS 3312 where the fluorescence signal can be combined with the aerodynamic size to obtain characteristic size distributions of bioaerosols (Ho et al., 1999). Biological particle growth has been observed (Madelin and Johnson, 1992). Several biological species were measured using the APS 3312 to evaluate the response (Brosseau et al., 2000). Differences in the fluorescence signals of biological particles versus non-fluorescent control particles were seen, but no relationship to culturability of the bacteria or fungi was found, and the differences in fluorescence signal could not be related to known bacterical species.

The APS has been applied to the measurement of penetration curves of several types of aerodynamic classification devices, such as impactors (Baron, 1983), cyclones (Kenny and Gussman, 1997; Chen et al., 1999; Maynard, 1999), and open-pore foams (Fabriés et al., 1998;

Chen et al., 1999). Systems optimized for measurement of penetration curves have been developed (John and Kreisberg, 1999; Maynard et al., 1999). The challenge aerosol for this type of measurement preferably consists of spherical particles with a density of approximately 1000 kg/m^3 [1 g/cm^3] and with a distribution centered near the 50% cutpoint of the classification device. There should be an adequate concentration of particles throughout the size range of measurement, with a minimal concentration in the 0.5 μm range, to reduce the effects of coincidence. The challenge aerosol concentration is generally optimal in the 2×10^{-5} to 1×10^{-4} particles/m^3 (20 to 100 particles/cm^3) range.

AEROSIZER

Principles of Measurement

The Aerosizer (***TSI***) is based on the acceleration of particles and TOF principles, although at higher particle acceleration than in either the E-SPART or APS. The idea of accelerating particles in a sonic expansion flow and measuring the terminal velocity was first proposed and demonstrated in laboratory prototype instruments by Dahneke and co-workers

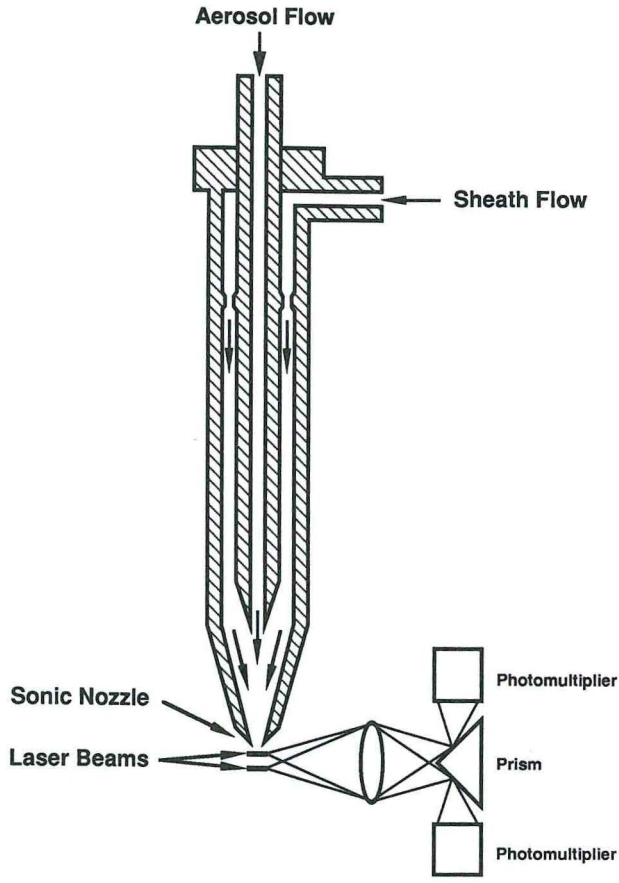

Fig. 17–13. Schematic of the detection system of the Aerosizer. The two laser beams are perpendicular to both the aerosol flow and detection direction.

(Dahneke, 1973; Dahneke and Padliya, 1977; Cheng and Dahneke, 1979; Dahneke and Cheng, 1979). The Aerosizer is the commercial product of this aerosol-beam research. Figure 17–13 depicts the particle-detection section of the device. The aerosol enters the inner capillary tube, surrounded by particle-free sheath air in the outer tube. Air and particles are accelerated through a convergent nozzle (0.75 mm diameter) with a 15° half angle and are delivered into a partially evacuated chamber. The ratio of pressure in the chamber and that in the ambient air is much smaller than 0.53; therefore, the air velocity at the nozzle exit, V_g, attains sonic velocity:

$$V_g = \sqrt{\frac{\gamma RT}{M}} \tag{17–34}$$

where γ is the ratio of specific heat capacities (1.4 for air), R is the gas constant, T is the temperature in K, and M is the molecular weight (28.96 for air). The air continues to expand in the chamber with a supersonic free-jet flow. The flow field in the convergent nozzle and the supersonic expansion have been described (Dahneke and Cheng, 1979). From numerical calculations, it has been shown that the particle attains a terminal velocity soon after exiting the nozzle (Dahneke and Cheng, 1979). At a distance of five nozzle diameters downstream of the nozzle, the calculated axial velocity is within about 2% of that at a distance of 50 diameters downstream.

The TOF of a particle is measured with two laser beams located close to the nozzle. As particles pass through the laser beams, the light scattered from the particles is detected and converted into electronic signals by two photomultiplier tubes (PMTs). The distance between the two laser beams is about 1 mm with about a 20 to 30 μm spread of the individual beams. One PMT detects light as the particle passes through the first beam, while the other PMT detects the light from the second beam. The time between these two events (TOF) is measured and recorded to an accuracy of ±25 ns. Each PMT converts the scattered light into an electrical pulse that is sent to the data-acquisition system. A low PMT threshold senses the weak pulses generated by small particles. However, at the low PMT threshold larger particles can cause the PMT to produce an electrical oscillation that generates multiple detected pulses from a single true pulse, a behavior called *ringing* (Thornburg et al., 1999). Therefore, the Aerosizer uses several PMT thresholds that are selected based on the initial pulse height so that spurious triggering on these subsequent oscillations does not occur.

Several models of the Aerosizer have been produced by Amherst Process Instruments, including the original Aerosizer, the Aerosizer LD, and the Aerosizer DSP. Amherst Process Instruments was purchased by ***TSI*** in 1999, and the DSP version was designated Model 3220 (***TSI***). The principal improvements differentiating the models were that the Aerosizer LD had the HeNe laser replaced by a LD light source and the DSP model had an improved signal processor to reduce spurious triggering due to noise and ringing in large particle signals.

Calibration with Spherical Particles

The terminal velocity and TOF are functions of particle diameter, density, shape, and ambient pressure. Calibration curves (Fig. 17–14) provided by the manufacturer are based on theoretical calculations and experimental data from solid spherical particles. The experimental validation of the calibration curves, also provided by the manufacturer, uses a limited number of monodisperse spherical particles of polystyrene latex (PSL) and glass. A more extensive calibration of the instrument requires both PSL (density = 1050 kg/m^3 [1.05 g/cm^3]) and glass (density = 2460 kg/m^3 [2.46 g/cm^3]) particles with a size range of 0.5 to 150 μm obtained at an ambient pressure of 0.82 and 1 atm. This work is shown in Figure 17–15 (Cheng et al., 1993). Calibration curves for particles of these densities were calculated from the Aerosizer calibration table using an interpolation method and are plotted along with the measured data

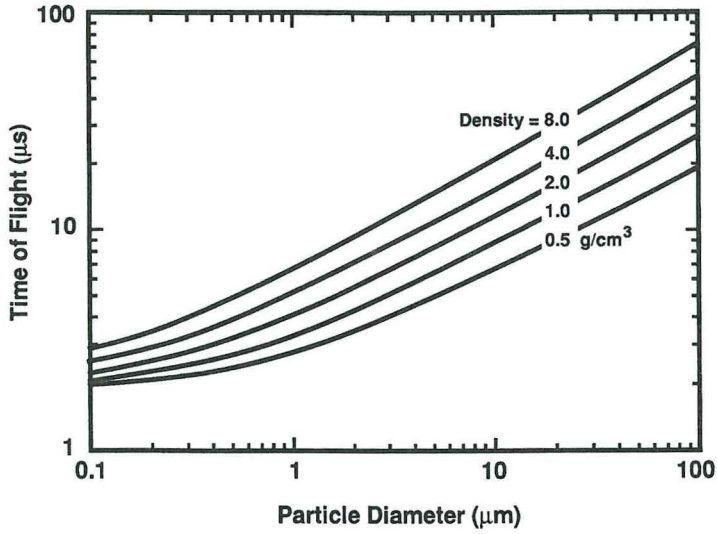

Fig. 17–14. Calculated Aerosizer calibration curves for spherical particles of different densities. (Courtesy of Amherst Process Instruments, Inc.)

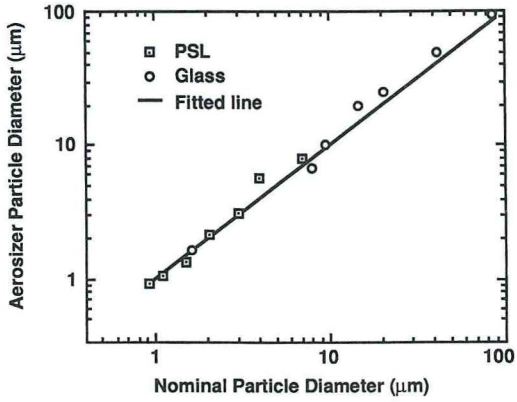

Fig. 17–15. Aerosizer calibration data for polystyrene latex (PSL) particles (density = 1050 kg/m^3 [1.05 g/cm^3]) and glass beads (density = 2450 kg/m^3 [2.45 g/cm^3]).

in Figure 17–15. Excellent agreement was found between the TOF of the PSL particles in the size range of 2 to 10 μm at 101.3 kPa [1 atm]. At a reduced pressure of 0.82 atm, the TOFs obtained for the PSL and glass particles were slightly higher than predicted by the calibration curves for the size range from 0.4 to 150 μm geometric diameter. However, the calibration tables were developed for normal ambient conditions, and theory predicts higher TOFs for operation under reduced ambient pressure (Dahneke and Cheng, 1979; Oskouie et al., 1998; Tsai et al., 1998); thus, the disagreement between the measured data and calibration curves was expected. The magnitude of the overestimation of particle size by the Aerosizer is expressed in terms of the ratio of the geometric diameter measured by the Aerosizer to the true geometric diameter from microscopy (d_{API}/d_g). This ratio took values between 1.08 and 1.27 for the PSL particles and glass beads.

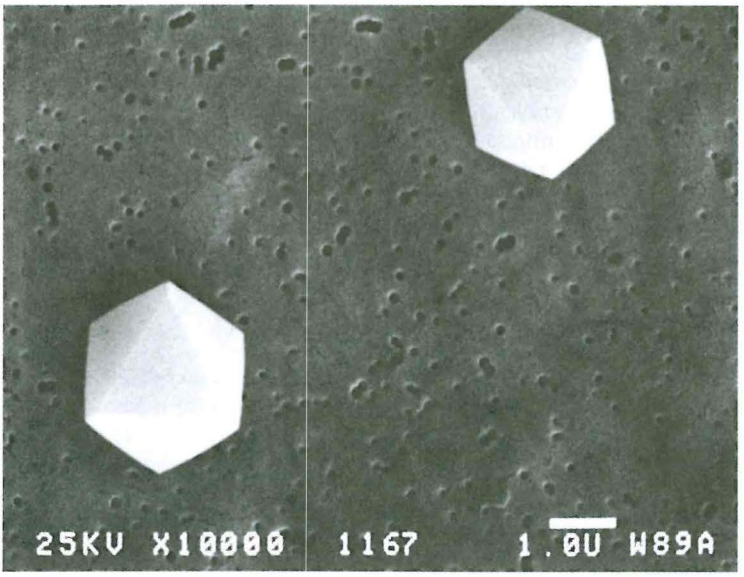

Fig. 17–16. Natrojarosite particles. (From Cheng et al., 1993, with permission.)

Tsai et al. (1998) calculated the particle trajectory assuming compressible flow in the Aerosizer nozzle, with a corresponding drag coefficient formula suitable for a range of Mach numbers and Reynolds numbers and appropriate for the Aerosizer operating conditions. The calculated TOF is in good agreement with experimental data obtained at 83.1 kPa [0.82 atm] pressure (Fig. 17–15). Compared with the calibration curve in Figure 17–14, the calculated results show deviation for particles greater than 10 μm. This deviation was due to the fact that Figure 17–14 was calculated assuming a one-dimensional flow field and a different formula for drag coefficient.

Instrument Responses with Nonspherical Particles and Droplets

Responses from the Aerosizer for nonspherical natrojarosite particles ($Na\ Fe_3[SO_4]_2\ [OH]_6$) were measured (Cheng et al., 1993). Preparation and characterization of the uniform-sized particles formed as single, symmetrical truncated cubes (Fig. 17–16) with a density of 3.11 g/cm^3 have been described (Marshall et al., 1991). Particles having sizes between 7.3 and 18.8 μm aerodynamic diameter were prepared and classified by aerodynamic size in a Timbrell spectrometer (see Chapter 10). Figure 17–17 presents plots of the Aerosizer-measured aerodynamic diameter against mean aerodynamic diameter. In all cases, the Aerosizer significantly undersized the natrojarosite particles, and the degree of size reduction was size dependent. Thus, the largest particles with true aerodynamic diameters close to 18.8 μm were undersized by as much as 51%, whereas the smallest particles analyzed with true aerodynamic diameters of 7.3 μm were undersized by only 21%.

Liquid droplets also behave differently from solid spherical particles in the Aerosizer. The Aerosizer underestimates the true aerodynamic diameter of oleic acid droplets (Tsai et al., 1998), similar to results shown by Baron (1986) and Bartley et al. (2000) from the APS. The deformation is a function of the Weber number (Baron, 1986; Lefebvre, 1989). A Weber number greater than the range of 12 to 20 suggest that the droplets broke up, whereas Weber numbers within that range indicate that the droplets may have deformed (Lefebvre, 1989). Calculations of Weber numbers for 1 and 5 μm oleic acid showed that particles larger than

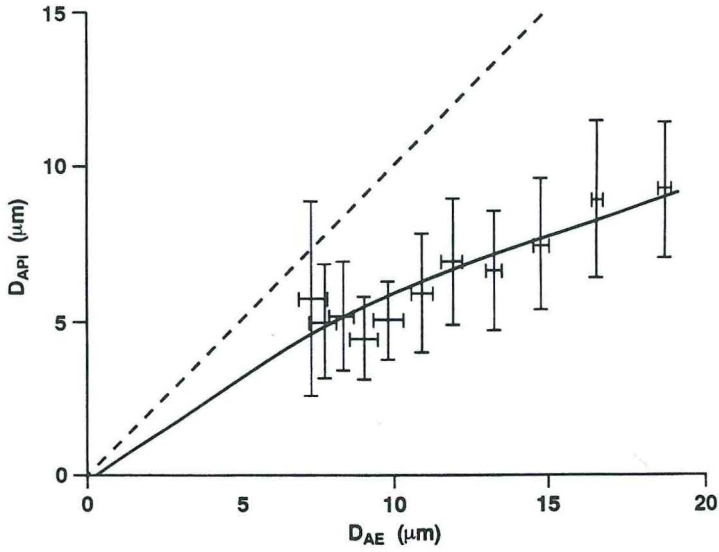

Fig. 17–17. Comparison between the Timbrell Spectrometer and the Aerosizer-measured aerodynamic diameters of natrojarosite at normal ambient pressure (100 kPa [750 mm]). (From Cheng et al., 1993, with permission.)

5 μm have Weber numbers in the 12 to 20 range and may deform in the measurement region (Thornburg et al., 1999). These results agree with experimental data showing particle deformation for oleic acid particles greater than 7 μm (Baron et al., 1996; Tsai et al., 1998). The Aerosizer is thus likely to exhibit a greater degree of droplet deformation than the APS due to its higher particle acceleration.

Transmission Efficiency

There are several reasons that some particles are not counted by the Aerosizer. The first is the transmission efficiency; the aerosol must penetrate the inlet nozzle and pass through the laser beams. Large particles may deposit in the inlet nozzle by impaction. After particles pass through the nozzle exit, small particles may follow the divergent gas streamline and fail to intercept the laser beams. Both scenarios result in lowered counting efficiency. In a numerical simulation, aerosol transmission efficiency in the Aerosizer was estimated by considering impaction in the nozzle, rebounding of solid particles, and passage through the sensing zone (Tsai et al., 1999). Theoretical calculations showed that the transmission efficiency is a complex function of particle size, beam diameter, and the solid or liquid state of the particle. For liquid particles at a typical laser beam diameter of 300 μm, the counting efficiency was about 4% for 0.1 μm particles, increasing to a maximum of about 27% for 2.5 to 3 μm particles. The counting efficiency decreased for larger particles due to deposition in the nozzle. For solid particles, the counting efficiency was essentially the same as for liquid particles in the size range of 1 to 10 μm. For particles greater than 10 μm, the counting efficiency increased further due to particle bounce in the inlet. The counting efficiencies were predicted to be higher for 600 and 800 μm diameter laser beams, suggesting that redesign of the detection optics would improve the instrument response.

The counting efficiency of the Aerosizer LD was determined experimentally using polydisperse oleic liquid droplets (Thornburg et al., 1999). The determination included effects of transmission efficiency and factors such as signal processing, where signals lower than the

threshold were not considered. The counting efficiency of the Aerosizer for 0.3 to 10 μm particles varied substantially with particle size, PMT voltage, and count rate. The counting efficiency was less than 1% for particles smaller than 0.5 μm, whereas efficiencies for particles greater than 7 μm occasionally exceeded 100%. The low efficiency for small particles was due to low light scattering intensity, and the artificially high counting efficiency for larger particles was due to the ringing effects of multiple signals from each pulse. The strong dependence of counting efficiency on particle size increased the median diameter of the size distribution. The Aerosizer DSP signal processing system may give substantially improved results (see below).

Coincidence Errors

At high concentrations, the counting efficiency may decrease due to several causes associated with the measurement process that result in undetected particles (Mitchell et al., 1999). First, the transit time of a particle through each laser beam along with the electronic counting dead time for each pulse determines the upper limit of particle detection. When more than one particle is present in the same beam during the first particle's presence, information about one particle is lost, decreasing the measured concentration.

Second, the operation of the particle-detection electronics may be as important as beam-residence coincidence in determining an upper concentration limit associated with an arbitrarily defined, acceptable level of accuracy. At least two potential sources of particle loss from this cause are known. The amount of dead time associated with the two PMTs that detect light scattered by particles as they interact with the "start" and "stop" laser beams can cause particles to be lost if a second particle arrives during the period of detector insensitivity. Dead times are 400 and 800 ns for the low-sensitivity (large particle) and high-sensitivity (small particle) detection systems, respectively. Based on these dead times, it follows that limiting particle concentrations are 1.5×10^{12} and 7.5×10^{11} particles/m^3 for the fine and coarse particle-detection systems, respectively. These limits are at least an order of magnitude larger than values of concentrations measured previously using the Aerosizer with some pharmaceutical aerosols (Mitchell and Nagel, 1996). Dead time coincidence is likely to contribute only a small error under these conditions.

The operation of the timers for the particle detection system may introduce a more significant bias in the accurate determination of concentration, as the duration of insensitivity to incoming particles under overloaded conditions can be close to two orders of magnitude longer. As each particle passes through each laser beam, the scattered light is detected and converted into either a low- or high-amplitude electrical signal by the "start" and "stop" PMTs. The low signal threshold is set at high sensitivity (high-gain region) to measure scattered light from small particles, and conversely the high-signal threshold is set at low sensitivity (low-gain region) to measure light scattered by large particles. Thus, the two PMTs allow a differentiation between the entry and exit pulses associated with each particle. However, instead of linking two adjacent "start" and "stop" pulses with each other to define the TOF for a given particle, the Aerosizer detection system considers all the pulses over a defined time period and correlates pulses of equal intensity to define the TOF of individual particles. Signals having unequal intensity are randomly combined and averaged into a background signal. These background "particles" are equivalent to the phantom particles produced by coincidence in the APS, but are routinely subtracted from the final spectrum.

In more detail, each sensitivity region of the Aerosizer LD has four timers, each of which remains in the ON condition for a maximum of 52 μs after being triggered by a detected particle before being automatically reset. A timer starts when a particle is detected by the "start" PMT. If additional particles arrive at the "start" laser beam before the first particle arrives at the "stop" beam, each particle starts an additional timer until all four timers are operating. When a particle reaches the "stop" beam, its pulse detected by the "stop" PMT is corre-

lated with as many pulses from the other timers that have been triggered. It follows that if a particle arrives after all four timers have been triggered and before any have been reset, its pulse is lost to the system and a real particle count has not been detected. This so-called timer unavailable coincidence becomes progressively worse as the incoming particle concentration increases.

The manufacturer has estimated particle detection losses from all causes in a simulation that is based on the behavior of perfectly monodisperse small (0.5 μm aerodynamic diameter) and large (5.0 μm aerodynamic diameter) particles delivered to the measurement zone at progressively increasing feed rates. If a 10% loss is arbitrarily deemed as the limit for acceptable bias in the measurement, it follows that the maximum aerosol concentration should not exceed approximately 1×10^{10} particles/m^3.

Signal Processing. There are two versions of the Aerosizer processing system. The significant difference between the signal processing in the older Aerosizer systems (e.g., Aerosizer LD) and the Aerosizer DSP systems is the introduction of an adaptive threshold system. Older Aerosizer LD systems used two detection thresholds ("high sensitivity" and "low sensitivity"), which were effectively fixed during a run (the PMT voltage, and thus the effective threshold, could be varied on a run-by-run basis). This usually resulted in "phantom particles" from multiple triggers caused by effects such as PMT afterpulsing and laser-beam fringes on large particles and also made it difficult to select a sensitivity setting appropriate for the sample(s) being run (especially for mixtures of large and small particles). Because these "phantom particles" were correlated with real particles, they showed up in the distribution as additional particles of approximately the same size as the real particles. These problems often produced significant errors in measured distributions (Heitbrink et al., 1991).

The Aerosizer DSP digitizes the PMT outputs and uses a digital delay line to allow the detection threshold to be dynamically set based on the behavior of the input signal. This delay line provides the ability to look "into the future" and thus set the thresholds based on how the signal will behave in the near term. These dynamic thresholds significantly improve the dynamic range of the detection process, providing the correlators with much better data from which to derive the TOF statistics.

Comparison Between the Aerosizer and the APS

Both the Aerosizer and the APS are based on the acceleration of particles in an aerosol beam and TOF measurement for size determination. However, the details of design and operation of these two instruments differ substantially. Whereas the APS is operated under subsonic flow with about 13.3 kPa [100 mm Hg] pressure differential between the ambient air and sensing volume (Chen et al., 1985), the Aerosizer is operated under supersonic conditions with a much higher pressure drop (greater than 100 kPa [750 torr] under 101.3 kPa [1 atm] ambient pressure). Therefore, a more powerful vacuum pump is needed for the Aerosizer, whereas the APS uses much smaller pumps placed inside the instrument. Because the nozzle in the Aerosizer is operated as a critical orifice, it controls the flow by itself. However, the APS requires a more elaborate flow-control system to keep a constant sampling flow rate. The Aerosizer has higher gas and particle velocities than the APS, for example, a 10 μm PSL particle attains about 100 m/s velocity in the Aerosizer versus about 38 m/s in the APS. With a higher velocity and therefore a higher Reynolds number in the Aerosizer, the drag force experienced by a particle will be higher than that in the Stokes regime ($Re < 0.1$). Therefore, the effects of particle density and shape factor on the instrument response will be greater in the Aerosizer than in the APS.

Another major difference between the Aerosizer and the APS is the method for measuring the TOF. The Aerosizer uses four timers for the TOF measurement. Only one clock is used in the APS to determine the TOF. This difference may be reflected in the noise level.

The noise of both instruments arises when the PMT produces a signal that is not associated with a particle event, and this signal is detected as a particle passing through the sensing volume. The calculated particle size from a false signal depends on the true particle concentration and the exact time sequence of this false signal. With a single clock system, the noise signals tend to produce more signals for small particles, whereas for the Aerosizer the noise level appears to be uniform across the size range. Both instruments have an internal mechanism to reduce or correct for the background noise level. However, it is not completely removed, and false signals affect the accuracy of the size distribution. Both the Aerosizer and the APS measure the size number distribution, but they also calculate the surface area and volume distributions, assuming that the particles are spherical. With noise corrections, false signals do not significantly affect the number distribution. However, when the same size distribution is transformed into a volume distribution, false signals in large particles are amplified. Therefore, the noise tends to skew the size distribution toward the large particles, especially in the Aerosizer.

The third feature of the Aerosizer that is different from the APS is the data presentation. Both instruments calculate the measured size distribution in terms of number, surface area, and volume distributions. The APS data are presented in the absolute units of particle number/cm^3, surface area/cm^3, and volume/cm^3, whereas the Aerosizer data are normalized with respect to the peak concentration. The Aerosizer distribution can be adjusted to give an estimated true concentration, but may be in error due to the way the background is subtracted from the TOF spectrum.

FIBROUS AEROSOL MONITOR

The measurement of fibers is useful for controlling the health risk due to exposure to airborne asbestos fibers and other similar materials. Currently, the most common method for estimating such exposure is personal filter cassette sampling followed by phase contrast light microscope counting of fibers. This method, exemplified by NIOSH Method 7400 (National Institute for Occupational Safety and Health, 1994), often requires sampling times of hours and analysis times of 5 to 20 min (see Chapters 12 and 26). The Fibrous Aerosol Monitor (originally model FAM-1, currently model FM-7400, ***MIE***) was developed under joint sponsorship of NIOSH, the Bureau of Mines, and the Environmental Protection Agency (Lilienfeld et al., 1979) to supplement this technique with real-time indication of fiber concentration.

The FAM preferentially detects fibers by aligning the fibers in an oscillating electric field, illuminating the fibers with a laser beam and detecting the resulting pulses of light with photomultiplier. Compact particles do not align in the oscillating field and thus do not produce pulses synchronous with the oscillating electric field.

Fiber Alignment

Particles in the sensing zone are subjected to a constant 300 V/mm electric field perpendicular to both the laser beam and the detector axis. A smaller ac field is applied at 45° to this field to oscillate the electric field in the ϕ direction (Fig. 17–18). With this field rocking motion, fibers aligned parallel to the electric field vector spend more time scattering light into the detector, thus improving sensitivity, than if the field exhibited a full 360° rotation (used in the prototype version).

Conductive fibers are predicted to align in the FAM with less than a 0.1° lag behind the rotating field (Lilienfeld, 1985). Nonconductive fibers are expected to align very poorly, if at all. Conductivity on the scale of fibers that are a few micrometers or tens of micrometers in length depends on surface conductivity as well as bulk conductivity. For instance, glass fibers have a very low bulk conductivity, but can align in the electric field of the FAM at a relative

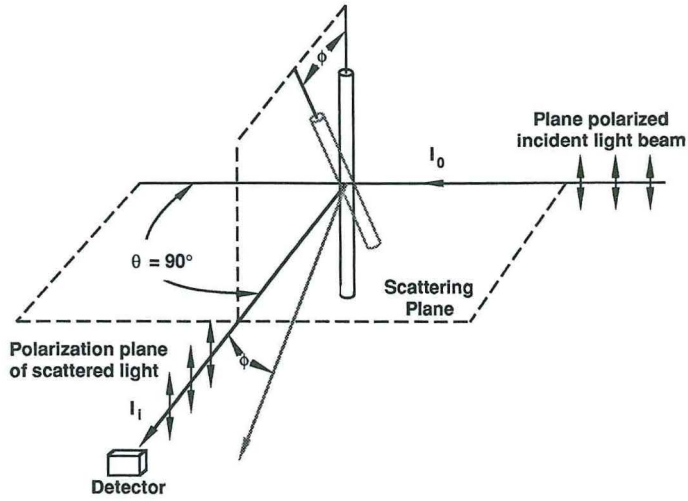

Fig. 17–18. Geometry of light scattering from a fiber in the Fibrous Aerosol Monitor (model FAM-1, MIE, Inc.). With the fiber perpendicular to the laser beam, the light scattered from the fiber occurs primarily in the plane perpendicular to both the fiber and the laser beam and results in a pulse of light reaching the detector as the fiber rotates. (Adapted from Lilienfeld, 1987.)

humidity above about RH 30%. Thus adsorbed water can provide enough surface conductivity to allow complete alignment. Asbestos fibers adsorb water more readily and align at much lower humidity levels.

Brownian motion can cause fibers to be randomly displaced from a fully aligned condition. At room temperature, the average angular deflection from alignment θ_B can be calculated from

$$\sin\theta_B \cong \frac{1}{\pi E}\sqrt{\frac{kT(\sin[2\beta]-1)}{2\varepsilon_o L^3}} \tag{17–35}$$

where E is the electric field, k is the Boltzmann constant, T is the absolute temperature, β is the fiber length-to-width (aspect) ratio, ε_o is the permittivity of free space, and L is the fiber length. The deflection is a strong function of fiber length, and, while fibers longer than 5 μm are predicted to align well in the FAM, shorter fibers may not hold alignment sufficiently well to be detected.

Sensing System

The FAM uses two fiber properties to exclude other types of particles: The alignment of conductive fibers with their long axis parallel to an electric field and the specific light-scattering pattern produced by fibers. A fiber in the FAM sensing zone is oriented by an electric field such that its fiber's major axis is always perpendicular to the incident light beam (Fig. 17–18). Under these conditions, the light scatters primarily into a plane that is perpendicular to the fiber axis and contains the light beam. The detector is situated to receive the maximum scattered light when the fiber is also perpendicular to the detector fiber axis. With very long fibers, this plane of scattering is quite thin. With a smaller length to diameter ratio, or aspect ratio, the scattering plane becomes broader, eventually approaching a uniform pattern as a function of ϕ for spherical particles. As with compact particles, more light is scattered in the

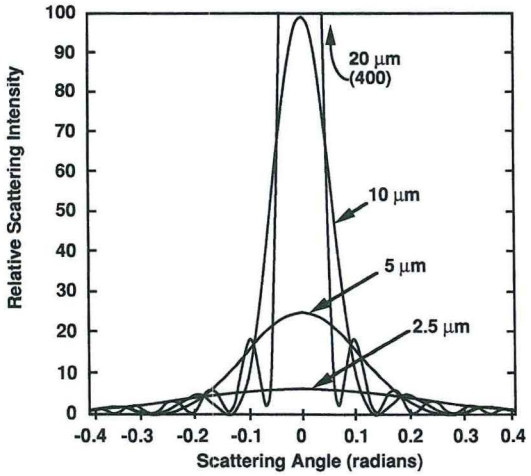

Fig. 17–19. Light-scattering pulses calculated for several fiber lengths for a single fiber diameter (Eq. 17–36). (Adapted from Lilienfeld, 1987.)

forward direction (small θ) than in the backward direction, and this proportion increases with fiber diameter. As with scattering from compact particles, the scattering intensity and angle dependence is a function of refractive index. The 90° detection angle in the FAM allows multiple detection of the same particle as it moves down the detection volume, improving sensitivity and specificity. In addition, for small-diameter fibers the scattered light tends to be plane-polarized parallel to the fiber axis. To increase the amount of scattered light from these fibers relative to that from nonaligned compact particles, a polarizing filter is placed in front of the photomultiplier detector.

A detector is placed at a right angle to the incident beam in the scattering plane as indicated in Figure 17–18. As a fiber rotates in the ϕ direction, a pulse of light is detected. The intensity profile of this pulse for small values of ϕ is indicated by

$$I \propto L^2 \left(\frac{\sin(\pi L \phi / \lambda)}{\pi L \phi / \lambda} \right)^2 \tag{17–36}$$

where I is the scattering intensity, L is the fiber length, and λ is the light wavelength (0.6328 μm) (Lilienfeld, 1987). The sharpness of the scattering pattern indicated by this function depends on the fiber length. Pulse sharpness is used as a discrimination in the FAM to limit the detection to fibers longer than 5 μm. The curves in Figure 17–19 indicate the relative scattering intensity profiles as calculated by Eq. 17–36 for fibers of several lengths. A calculation of the sensitivity of the FAM indicates that it is capable of detecting 0.075 μm diameter fibers that are longer than 5 μm (Lilienfeld, 1987).

Nonideal Fiber Behavior

The theoretical considerations that are the basis for the fiber alignment and detection system in the FAM assume that ideal cylindrical fibers are being detected. However, there are a number of factors that can make fiber detection difficult to characterize theoretically. For instance, fibers may not have the ideal cylindrical or even an ellipsoidal shape. Asbestos fibers are typically bundles of fibrils that may have splayed ends, noncylindrical cross section, cur-

vature, attached particles, and so forth. Fibers may exist as clumps of multiple fibers floating in the air. Different fiber types have different refractive indices and hence different scattering efficiencies. Fibers with curvature or with other particles attached may not align at 90° to the detector axis to give optimum detection geometry.

The fibers of one of the most common types of asbestos, chrysotile, often exhibit curvature. This curvature was found to result in lower sensitivity in the FAM prototype (Lilienfeld et al., 1979). However, by applying a sufficiently high voltage field in the detection volume the fibers can be straightened so that they produce responses similar to more ideal fibers (Lilienfeld, 1985).

The laser beam does not uniformly illuminate the detection volume. The profile of the beam is Gaussian, indicating that fibers at the edge of the beam will scatter less light than fibers in the center of the beam. Large-diameter fibers may settle enough to be incompletely detected. In addition, charged fibers may drift away from the beam due to the high electric field. All these factors will affect the sensitivity and response of the instrument. Thus, as with other light-scattering instruments, a calibration procedure is required to make the instrument respond in a manner equivalent to light microscopic detection.

Instrument Characteristics

Sampling System. The airflow in the FAM is controlled by a diaphragm pump to $3.33 \times 10^{-5}\,m^3/s$ [2 L/min]. A 25 mm cellulose ester filter collects fibers that have been detected by the FAM; this filter can be used to check the FAM calibration. An adjustment to the pump voltage allows calibration of the flow rate. The aerosol enters a 12.7 mm diameter tube inlet and passes through two right-angle bends. This arrangement is required by laser safety regulations to prevent direct viewing of the laser beam. The aerosol flow continues down the 10 mm diameter sensing tube to the sensing volume and then out of the other end of the sensing tube (Fig. 17–20). A minor amount of clean air flow from the pump through the beam

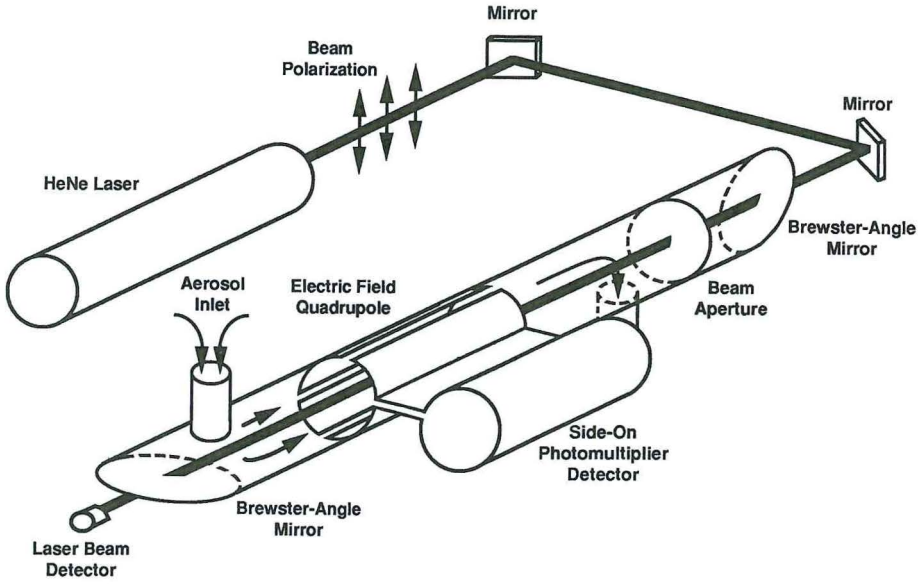

Fig. 17–20. Sensing system of the FAM-1, including the light-scattering system, fiber alignment system, and air flow pattern. (Adapted from Lilienfeld, 1987.)

orifice keeps the Brewster angle window (used to prevent backscatter of light) and orifice clean.

An additional option is available with the FAM that uses a virtual impactor to remove particles larger than 3 μm aerodynamic diameter from the sampled air stream. The impactor is driven entirely by the flow into the FAM inlet. The jet pressure in the impactor forces 10% of the flow with the large particles into the minor flow orifice, through a glass fiber filter, and through a rotameter. This 10% is thus impacted, filtered, and returned to the major flow entering the FAM. This arrangement has the advantage that an additional pump to control the minor flow is not required. With 10% of the small particles removed as well as the large particles, the final fiber count must be increased to adjust for this 10% loss.

The sensing volume is far enough downstream from the inlet that laminar flow is established. Under these conditions, the fibers are expected to align parallel to the flow until they reach the sensing zone. As indicated in Figure 17–20, the laser beam shines down the center of the sensing tube so only those fibers in the center, illuminated by the beam, are detected. In addition, fibers must stay in the beam for a sufficient time to be recorded as a fiber. Thus, any fibers that settle or otherwise deviate more than a fraction of the beam radius (about 0.7 mm) in a straight trajectory in the 0.1 s it takes the fiber to traverse the sensing zone will not be recorded as a fiber.

As with other particle counters, the FAM exhibits coincidence errors at high fiber concentrations. Coincidence of two fibers in the detection volume results in only one fiber being counted. The coincidence level can be estimated using Eq. 17–33 with a detection volume ($Q \cdot t$) of 8.3 mm^3. This indicates a coincidence loss of about 15% at a measured concentration of 15×10^6 fibers/m^3 [15 fibers/cm^3].

The FAM is a small suitcase-sized instrument with a mass about 12 kg and is normally operated from 115 V ac power, although a battery pack option is available that allows up to 3 h of operation. The readout is by liquid crystal display in fibers/cm^3. The FM-7400 has several outputs for data recording and calculates several statistics to indicate when a selected threshold has been reached with reasonable confidence. An alarm feature also indicates when the concentration exceeds a selected value. The pulse width of the signal is analyzed to estimate fiber length according Eq. 17–36 so that fiber length distributions in the range of approximately 2 to 300 μm can be measured.

Calibration

The original aim in the development of the FAM was to provide a real-time direct-reading monitor capable of giving fiber concentrations equivalent to those provided by the reference method using filter sample collection and phase contrast light microscope analysis (e.g., NIOSH Method 7400, as described in Chapters 12 and 23). Because the instrument response cannot be predicted theoretically, it must be calibrated by a side-by-side comparison with the reference method. Each instrument is calibrated in this fashion by the manufacturer with an amosite aerosol produced from a vibrating fluidized bed generator. During calibration, the instrument and filter inlets are placed close together. Most asbestos fibers from the generator have small enough Stokes numbers not to be significantly affected by anisokinetic sampling.

The instrument detection thresholds (for pulse height and sharpness) are set such that the measurement rate is effectively 167 mm^3/s [10 cm^3/min]. This is the flow rate through the laser beam in the sensing region. The FAM was originally designed to measure concentrations at levels near the U.S. asbestos standard in 1978, namely, 2×10^6 fiber/m^3 [2 fibers/cm^3]. The permissible exposure limit in workplaces is currently 1×10^5 fiber/m^3 [0.1 fibers/cm^3]. This sensor flow rate requires relatively long sample times to obtain good confidence in the results at low concentrations, for example, at a concentration of 10^5 fiber/m^3 [0.1 fibers/cm^3], 100 fibers are counted in 100 min.

FAM Evaluations and Application

A number of studies have been performed on the FAM, although most of these have not been in-depth evaluations. In general, these studies indicated that the FAM provides comparable results to the reference method. An evaluation was carried out by Iles and Shenton-Taylor (1986) that indicated good correlation of laboratory measurements with the reference phase contrast method, but field measurements gave much poorer agreement. The FAM manufacturer indicated that this study may have suffered from poor reliability of the instrument. It was found that instruments constructed in the first several years of production were notoriously unreliable, primarily because of the ease of laser misalignment. Improvements in the instrument ruggedness largely eliminated these and other stability problems. However, no further detailed studies of the FAM have been carried out since the mid-1980s.

The FAM was used as a monitor for asbestos removal operations. The FAM provided real-time indication of fiber concentrations inside and outside these sites to ensure the integrity of the asbestos aerosol containment system. Because the filter sampling typically takes an hour or more with filter analysis adding at least another 30 min, the FAM provided much more rapid feedback to prevent unnecessary exposure to potentially high concentrations of asbestos aerosols.

REFERENCES

Agarwal, J. K. and R. J. Remiarz. 1981. *Development of an Aerodynamic Particle Size Analyzer.* USDHEW-NIOSH Contract Report No. 210-80-0800. Cincinnati, OH: NIOSH.

Ananth, G. and J. C. Wilson. 1988. Theoretical analysis of the performance of the TSI aerodynamic particle sizer. *J. Aerosol Sci.* 9:189–199.

Baron, P. 1983. *Sampler Evaluation with an Aerodynamic Particle Sizer.* International Symposium on Aerosols in the Mining and Industrial Work Environment. Minneapolis, MN: Ann Arbor Press.

Baron, P. A. 1986. Calibration and use of the aerodynamic particle sizer (APS 3300). *Aerosol Sci. Technol.* 5(1):55–67.

Baron, P. A. and K. Willeke. 1986. Respirable droplets from whirlpools: Measurements of size distribution and estimation of disease potential. *Environ. Res.* 39:8–18.

Baron, P. A., J. M. Yacher, and W. A. Heitbrink. 1996. *Some Observations on the Response of the Aerosizer to Droplets in the 4–18 μm Range.* Presented at the American Association for Aerosol Research Annual Conference, Orlando, FL.

Bartley, D. L., P. A. Baron, A. B. Martinez, D. R. Secker, and E. Hirsch. 2000. Droplet distortion in accelerating flow. *J. Aerosol Sci.* 31:1447–1460.

Brockmann, J. E. and D. J. Rader. 1990. APS response to nonspherical particles and experimental determination of dynamic shape factor. *Aerosol Sci. Tech.* 13:162–172.

Brosseau, L. M., D. Vesley, N. Rice, K. Goodell, M. Nellis, and P. Hairston. 2000. Differences in detected fluorescence among several bacterial species measured with a direct-reading particle sizer and fluorescence detector. *Aerosol Sci. Technol.* 32(6):545–558.

Chen, B. T., Y. S. Cheng, and H. C. Yeh. 1985. Performance of a TSI aerodynamic particle sizer. *Aerosol Sci. Technol.* 4:89–97.

Chen, B. T., Y. S. Cheng, and H. C. Yeh. 1990. A study of density effect and droplet deformation in the TSI aerodynamic particle sizer. *Aerosol Sci. Technol.* 12:278–285.

Chen, C.-C., C.-Y. Lai, T.-S. Sheng, and J.-S. Hwang. 1999. Laboratory performance comparison of respirable samplers. *Am. Ind. Hyg. Assoc. J.* 60(5):601–611.

Cheng, Y. S., E. B. Barr, I. A. Marshall, and J. P Mitchell. 1993. Calibration and performance of an API Aerosizer. *J. Aerosol Sci.* 24:501–514

Cheng, Y. S., B. T. Chen, and H. C. Yeh. 1990. Behavior of isometric nonspherical aerosol particles in the aerodynamic particle sizer. *J. Aerosol Sci.* 21(5):701–710.

Cheng, Y. S. and B. E. Dahneke. 1979. Properties of continuum source particle beams. II. Beams generated in capillary expansions. *J. Aerosol Sci.* 10:363–368.

Clift, R., J. R. Grace, and M. E. Weber. 1978. *Bubbles, Drops and Particles*. New York: Academic Press.

Cole, K. R. 1999. *High Precision Micromotion Aerosol Spectrometry*. Ph.D. Dissertation. University of Arkansas, Little Rock.

Cole, K. R. and K. B. Tennal. 1993. Acoustic measurement of aerosol particles. *Aerosol Sci. Tech.* 19: 339–350.

Dahneke, B. 1973. Aerosol beam spectrometry. *Nature Physical Sci.* 244:54–55.

Dahneke, B. E. and Y. S. Cheng. 1979. Properties of continuum source particle beams I. Calculation methods and results. *J. Aerosol Sci.* 10:257–274.

Dahneke, B. and D. Padliya. 1977. Nozzle-inlet design for aerosol beam. *Instruments in Rarefied Gas Dynamics*, 51, Part II, pp. 1163–1172.

Fabriés, J. F., P. Görner, E. Kauffer, R. Wrobel, and J. C. Vigneron 1998. Personal thoracic CIP10-T sampler and the static version CATHIA-T. *Ann. Occup. Hyg.* 42(7):453–466.

Fuchs, N. A. 1964. *Mechanics of Aerosols.* New York: Pergamon Press.

Griffiths, W. D., P. J. Iles, and N. P. Vaughan. 1986. The behaviour of liquid droplet aerosols in an APS3300. *J. Aerosol Sci.* 17(6):921–930.

Heitbrink, W. A., P. A. Baron, and K. Willeke. 1991. Coincidence in time-of-flight spectrometers: Phantom particle creation. *Aerosol Sci. Technol.* 14:112–126.

Ho, J., M. Spence, and P. Hairston. 1999. Measurement of biological aerosol with a fluorescent aerodynamic particle sizer (FLAPS): Correlation of optical data with biological data. *Aerobiologia.* 15:281–291.

Iles, P. J. and T. Shenton-Taylor. 1986. Comparison of a fibrous aerosol monitor (FAM) with the membrane filter method for measuring airborne asbestos concentrations. *Ann. Occup. Hyg.* 30(1):77–87.

John, W. and N. Kreisberg. 1999. Calibration and testing of samplers with dry, polydisperse latex. *Aerosol Sci. Technol.* 31(2–3):221–225.

Kenny, L. C. and R. A. Gussman. 1997. Characterization and modelling of a family of cyclone aerosol preseparators. *J. Aerosol Sci.* 28(4):677–688.

Kinney, P. D. 1990. *Inlet efficiency study for the TSI Aerodynamic Particle Sizer*. M.S. thesis. Department of Mechanical Engineering, University of Minnesota.

Kinney, P. D., D. Y. H. Pui, and D. B. Blackford. 1989. *Particle sizing resolution and transmission efficiency of several inlet designs for the TSI Aerodynamic Particle Sizer*. American Association for Aerosol Research Annual Meeting, Reno, Available from TSI.

Lee, K. W., J. C. Kim, and D. S. Han. 1990. Effects of gas density and viscosity on response of Aerodynamic Particle Sizer. *Aerosol Sci. Technol.* 13:203–212.

Lefebvre, A. H. 1989. *Atomization and Sprays*. Bristol, PA: Taylor and Francis.

Lilienfeld, P. 1985. Rotational electrodynamics of airborne fibers. *J. Aerosol Sci.* 16(4):315–322.

Lilienfeld, P. 1987. Light scattering from oscillating fibers at normal incidence. *J. Aerosol Sci.* 18(4):389.

Lilienfeld, P., P. Elterman, and P. Baron. 1979. Development of a prototype fibrous aerosol monitor. *Am. Ind. Hyg. Assoc. J.* 40(4):270–282.

Madelin, T. M. and H. E. Johnson. 1992. Fungal and *Actinomycete* spore aerosols measured at different humidities with an aerodynamic particle sizer. *J. Appl. Bacteriol.* 72(5):400–409.

Marshall, I. A., J. P. Mitchell, and W. D. Griffiths. 1991. The behaviour of regular-shaped nonspherical particles in a TSI aerodynamic particle sizer. *J. Aerosol Sci.* 22(1):73–89.

Maynard, A. D. 1999. Measurement of aerosol penetration through six personal thoracic samplers under calm air conditions. *J. Aerosol Sci.* 30(9):1227–1242.

Maynard, A. D., L. C. Kenny, and P. E. J. Baldwin. 1999. Development of a system to rapidly measure sampler penetration up to 20 μm aerodynamic diameter in calm air using the Aerodynamic Particle Sizer. *J. Aerosol Sci.* 30(9):1215–1226.

Mazumder, M. K., N. Grable, Y. Tang, S. O'Connor, and R. A. Sims. 1999. Real-time particle size and electrostatic charge distirubtion analysis and its applications to electrostatic processes. *Inst. Phys. Conf. No. 163*, pp. 335–347.

Mazumder, M. K. and K. J. Kirsch. 1977. Single particle aerodynamic relaxation time analyzer. *Rev. Sci. Instrum.* 48(4):622.

Mazumder, M. K., R. E. Ware, and W. G. Hood. 1983. Simultaneous measurements of aerodynamic diameter and electrostatic charge on single-particle basis. In *Measurements of Suspended Particles by Quasi-Elastic Light Scattering*, ed. B. Dahneke. New York: John Wiley & Sons.

Mazumder, M. K., R. E. Ware, J. D. Wilson, R. G. Renninger, F. C. Hiller, P. C. McLeod, R. W. Raible, and M. K. Testerman. 1979. SPART analyzer: Its application to aerodynamic size distribution measurements. *J. Aerosol Sci.* 10:561–569.

Mazumder, M. K., R. E. Ware, T. Yokoyama, B. J. Rubin, and D. Kamp. 1991. Measurement of particle size and electrostatic charge distributions on toners using E-SPART analyzer. *IEEE Trans. Ind. Appl.* 27(4):611–619.

Mitchell, J. P. and M. W. Nagel. 1996. An assessment of the API Aerosizer for the real time measurement of medical aerosols from the pressurized metered-dose inhaler system. *Aerosol Sci. Technol.* 25: 411–423.

Mitchell, J. P., M. W. Nagel, and Y. S. Cheng. 1999. Use of the Aerosizer aerodynamic particle size analysis to characterize aerosols from pressurized metered-dose inhalers (pMDIs) for medication delivery. *J. Aerosol Sci.* 30:467–477.

National Institute for Occupational Safety and Health. 1994. Fibers, Method 7400 Issue No. 2 (8/15/94). *NIOSH Manual of Analytical Methods*. Cincinnati, OH: DHHS (NIOSH). Pub. No. 84–100.

Oskouie, A. K., H.-C. Wang, R. Mavliev, and K. E. Noll. 1998. Calculated calibration curves for particle size determination based on time-of-flight (TOF). *Aerosol Sci. Technol.* 29(5):433–441.

Peters, T. M., H. M. Chein, D. A. Lundgren, and P. B. Keady. 1993. Comparison and combination of aerosol size distributions measured with a low pressure impactor, differential mobility particle sizer, electrical aerosol analyzer, and aerodynamic particle sizer. *Aerosol Sci. Technol.* 19(3):396–405.

Rader, D. J., J. E. Brockmann, D. L. Ceman, and D. A. Lucero. 1990. A method to employ the APS factory calibration under different operating conditions. *Aerosol Sci. Technol.* 13(4):514–521.

Remiarz, R. J., J. K. Agarwal, F. R. Quant, and G. J. Sem. 1983. Real-time aerodynamic particle size analyzer. In *Aerosols in the Mining and Industrial Work Environments*, Vol. 3, eds. V. A. Marple and B. Y. H. Liu. Ann Arbor, MI: Ann Arbor Science.

Renninger, R. G., M. K. Mazumder, and M. K. Testerman. 1981. Particle sizing by electrical single particle aerodynamic relaxation time analyzer. *Rev. Sci. Instrum.* 52(2):242.

Sioutas, C., E. Abt, J. M. Wolfson, and P. Koutrakis. 1999. Evaluation of measurement performance of the scanning mobility particle sizer and aerodynamic particle sizer. *Aerosol Sci. Technol.* 30(1):84–92.

Szewczyk, K., M. Lehtimaki, K. Willeke, D. E. Elliot, and W. L. Muth 1992. Measurement of the change in aerosol size distribution with bacterial growth in a pilot scale fermentor. *Biotech. Bioeng.* 39: 243–245.

Thornburg, S., J. Cooper, and D. Leith. 1999. Counting efficiency of the API Aerosizer. *J. Aerosol Sci.* 30:479–488.

Tsai, C. J., H. M. Chein, S. T. Chang, and J. Y. Kuo. 1998. Performance evaluation of an API Aerosizer. *J. Aerosol Sci.* 29:839–853.

Tsai, C. J., W. S. Yang, W. W. Szymanski, and H. M. Chein. 1999. Particle transmission efficiency through the nozzle of the API Aerosizer. *J. Aerosol Sci.* 30:1019–1028.

TSI, Inc. 1987. *Model APS33B System Aerodynamic Particle Sizer Instruction Manual.* TSI, Inc., St. Paul, MN.

Wake, D. 1989. Anomalous effects in filter penetration measurements using the aerodynamic particle sizer (APS 3300). *J. Aerosol Sci.* 20(1):13–17.

Wang, H. and W. John. 1989. A simple iteration procedure to correct for the density effect in the Aerodynamic Particle Sizer. *Aerosol Sci. Technol.* 10:501–505.

Wang, J. C. and W. John. 1987. Particle density correction for the Aerodynamic Particle Sizer. *Aerosol Sci. Technol.* 6:191–198.

Willeke, K. and B. Y. H. Liu. 1976. Single particle optical counter: Principles and application. In *Fine Particles: Aerosol Generation. Measurement, Sampling and Analysis*, ed. B. Liu. New York: Academic Press.

Wilson, J. C. and B. Y. H. Liu. 1980. Aerodynamic particle size measurement by laser-Doppler velocimetry. *J. Aerosol Sci.* 11(2):139–150.

Ye, Y. and D. Y. H. Pui. 1990. Particle deposition in a tube with an abrupt contraction. *J. Aerosol Sci.* 21(1):29–40.

AEROSOL MEASUREMENT

Principles, Techniques, and Applications

SECOND EDITION

Edited by

Paul A. Baron, Ph.D.
Physical Scientist
Centers for Disease Control and Prevention
National Institute for Occupational Safety and Health
Cincinnati, OH

Klaus Willeke, Ph.D.
Professor
Department of Environmental Health
University of Cincinnati
Cincinnati, OH

WILEY-INTERSCIENCE

A JOHN WILEY & SONS, INC., PUBLICATION

New York • Chichester • Weinheim • Brisbane • Singapore • Toronto

This book is printed on acid-free paper. ♾

Published simultaneously in Canada.

Library of Congress Cataloging-in-Publication Data:

Aerosol measurement : principles, techniques, and applications / [edited] by Paul A. Baron and Klaus Willeke.—2nd ed.

p. cm.

Includes index.

ISBN 0-471-35636-0 (cloth)

1. Aerosols—Measurement. 2. Air—Pollution—Measurement. I. Baron, Paul A., 1944– II. Willeke, Klaus.

TD884.5 .A33 2001

628.5'3'0287–dc21 2001017845

Printed in the United States of America.

10 9 8 7 6 5 4 3 2 1